AD NUMBER

AD871218

NEW LIMITATION CHANGE

TO

Approved for public release, distribution unlimited

FROM

Distribution authorized to U.S. Gov't. agencies only; Critical Technology; MAY 1970. Other requests shall be referred to Space and Missile Systems Organization, Attn: SMYSE, Norton AFB, CA 92409.

AUTHORITY

SAMSO USAF ltr, 21 Oct 1976

SAMSO-TR-70-142

A STUDY OF DROP BREAKUP BEHIND STRONG SHOCKS WITH APPLICATIONS TO FLIGHT

FINAL REPORT

Prepared by

AVCO GOVERNMENT PRODUCTS GROUP
AVCO SYSTEMS DIVISION
201 Lowell Street
Wilmington, Massachusetts 01887

AVSD-0110-70-RR
Contract F04701-68-C-0035

May 1970

Prepared for

SPACE AND MISSILE SYSTEMS ORGANIZATION
DEPUTY FOR REENTRY SYSTEMS
AIR FORCE SYSTEMS COMMAND
Norton Air Force Base, California 92409

FOR OFFICIAL USE ONLY

This document consists of 68 pages,
75 copies, Series A

SAMSO-TR-70-142

A STUDY OF DROP BREAKUP BEHIND STRONG SHOCKS WITH APPLICATIONS TO FLIGHT

FINAL REPORT

Prepared by

AVCO GOVERNMENT PRODUCTS GROUP
AVCO SYSTEMS DIVISION
201 Lowell Street
Wilmington, Massachusetts 01887

AVSD-0110-70-RR
Contract F04701-68-C-0035

by

W. G. Reinecke
and
G. D. Waldman

May 1970

APPROVED

T. R. Munson, Manager
Environmental Technology Programs

Prepared for

SPACE AND MISSILE SYSTEMS ORGANIZATION
DEPUTY FOR REENTRY SYSTEMS
AIR FORCE SYSTEMS COMMAND
Norton Air Force Base, California 92409

FOREWORD

This report was prepared by Avco Corporation under Air Force Contract F04701-68-C-0035. The effort reported here is in support of the ABRES program and covers experimental and analytical studies of water droplet interactions with reentry body flow fields.

This document is subject to special export controls and each transmittal to foreign governments or foreign nationals may be made only with prior approval of Space and Missile Systems Organization (SMYSE), Norton Air Force Base, California, 92409.

Information in this report is embargoed under the Department of State International Traffic in Arms Regulations. This report may be released to foreign governments by departments or agencies of the U. S. Government subject to approval of Space and Missile Systems Organization (SMYSE), Los Angeles AFS, California, or higher authority within the Department of the Air Force. Private individuals or firms require a Department of State export license.

This technical report has been reviewed and is approved.

Capt. L. Hillebrand
Project Officer, SMYSE
Air Force Systems Command
Norton Air Force Base, California

ABSTRACT

An experimental program has been carried out to determine the modes of raindrop breakup in air after passage of a strong shock wave. Relevant dimensionless parameters have been determined, and the experimental data have been correlated in terms of these parameters. The resulting correlations have been used to determine raindrop breakup in the shock layer of a reentering vehicle passing through a rainstorm.

EDITED BY:
EDITORIAL SERVICES SECTION
W. H. Barber

CONTENTS

ILLUSTRATIONS

ILLUSTRATIONS (Concl'd)

-x-

1.0 INTRODUCTION

If a reentry vehicle flying through the earth's atmosphere traverses a rainstorm, the raindrops striking the body surface at high speed may cause serious damage. This damage will be partially alleviated, however, by the presence of the flow field around the body.

Because the relative velocity between the rain drops and the flow near the body is high, the drops are decelerated and deflected away from the surface, and there is a tendency for the drops to shatter or to be stripped of part of their mass as they traverse the severe environment of the shock layer. In the latter case, the drops may be broken into droplets so small that they conform to the local streamlines in the shock layer and thus never hit the body surface.

Seen in drop-fixed coordinates, the stationary drop is overtaken by the bow shock wave of the vehicle, and the flow behind that shock wave (in the vehicle shock layer) fragments the drop. This view of the problem suggested that an experimental study of the shattering could be conducted in a shock tube. Such experiments are reported herein along with supporting analysis and application to a flight case.

Briefly, the purposes of the study were as follows: First, to determine experimentally the time after passage at which the drop was entirely shattered; second, to determine experimentally the drop mass as a function of time after shock passage and until complete breakup; third, to conduct sufficient analysis to allow general application of the experimental data; and finally, to show how the experimental and analytical results could be applied to actual flight.

To make the experiments realistic, the tests were conducted with shock Mach numbers of 3, 6, 9, and 11 at pressure altitudes of sea level, 20 kft, and 40 kft, respectively. The corresponding initial pressures were 760, 350, and 140 mm Hg. Water drop diameters employed varied from 0.5 to 2.5 mm, a range that is representative of naturally occurring rain drops. The experimental data are tabulated in the appendix.

2.0 EXPERIMENTS

2.1 EXPERIMENTAL APPARATUS

The test facility employed in this water droplet breakup study was a 1½-inch-diameter shock tube capable of attaining shock Mach numbers up to 12. A controlled stream of water droplets was introduced into the tube through the test section located at the end of the driven tube. The test section was equipped with viewing ports through which single-frame, flash X-ray or spark shadowgraph photographs were obtained at times varying from droplet/shock wave intercept to disintegration. A schematic of the facility, shown in Figure 1a, indicates the location of the various speed and pressure monitoring components. A closeup photograph of the test section assembly and drop generator is presented in Figure 1b.

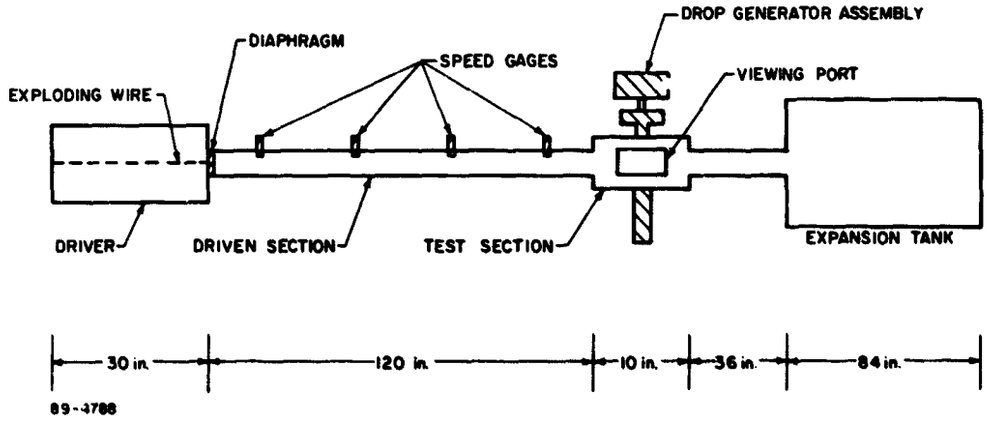

Figure 1a SCHEMATIC OF TEST FACILITY

The shock tube utilizes a 30-inch-long driver coupled to a 10-foot-long driven section between which is located a steel-petal-type diaphragm, scored to rupture at a predetermined pressure. The tube is operated using either a cold hydrogen or a combustion drive to cover the range of shock Mach numbers required. In the cold hydrogen mode, the gas was fed manually at a very slow rate into the driver until the diaphragm ruptured. Shock speeds up to Mach 3 were attained using this mode. To attain shock Mach numbers between 6 and 12, it was necessary to employ the combustion drive mode. A stoichiometric mixture of hydrogen and oxygen with a 70 percent helium dilution was ignited by an electrically exploded 2-mil-diameter aluminum wire producing driver pressures up to 14,000 psia. A driver pressure record obtained using a Kistler piezo-electric transducer is shown in Figure 2a indicating a slow burning rate. Occasionally very fast burning rates were obtained as shown in Figure 2b, resulting in a substantial change in shock speed. The variation in burning rates was attributed to the random mode in which the wire exploded as well as the degree of mixing of the three gaseous components. Generally, the fast burning mode resulted in unsatisfactory test conditions.

The test section located at the end of the driven tube was equipped with orthogonal ports; one set for introducing and catching the droplet stream, the other

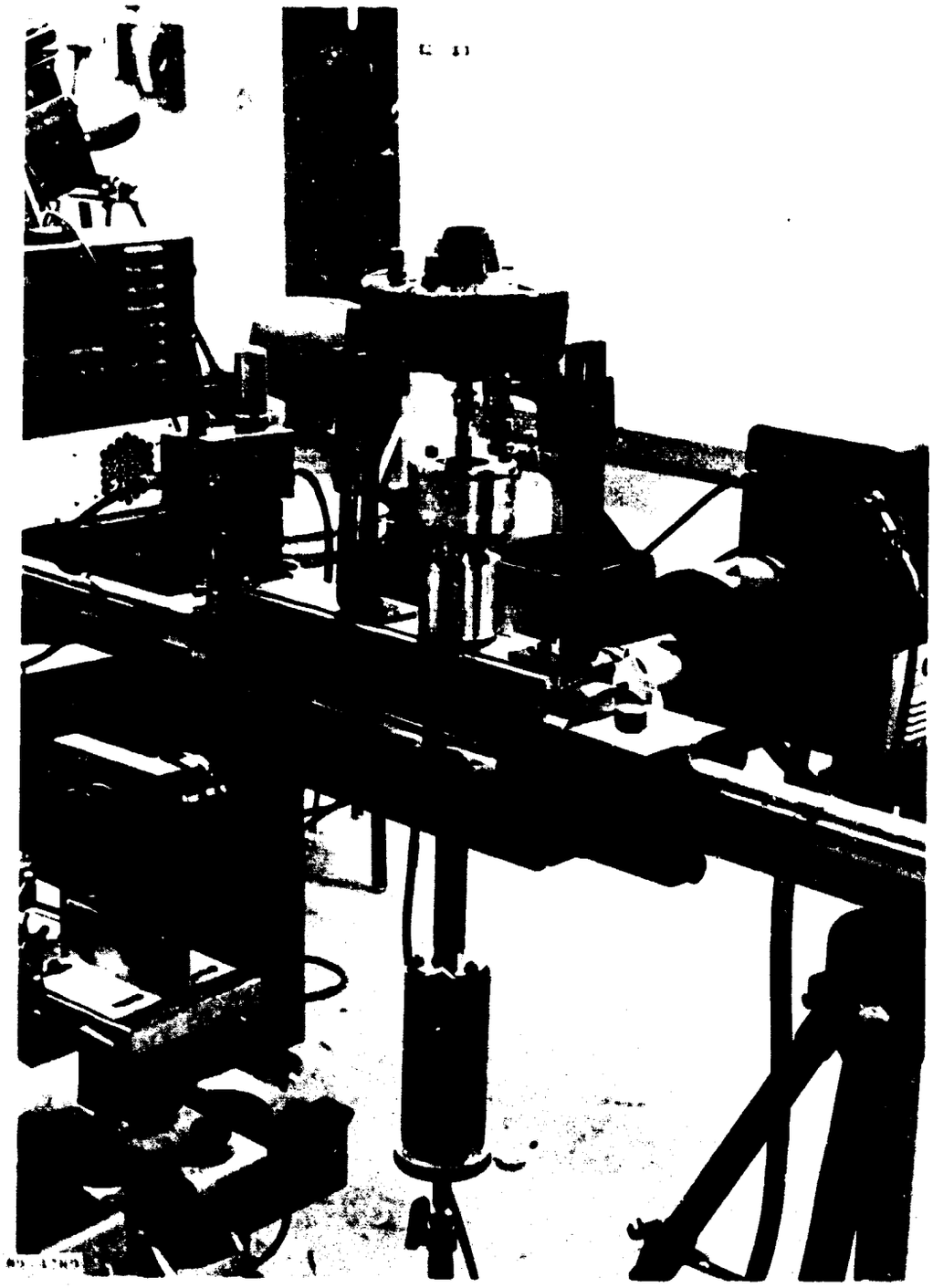

Figure 1: PHOTOGRAPH OF TEST FACILITY

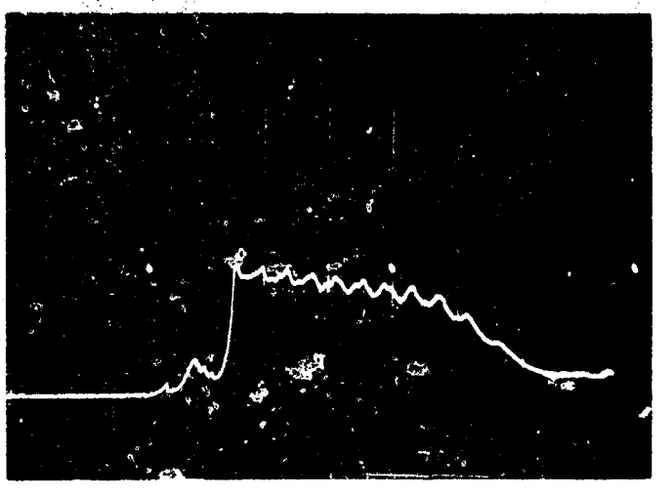

Figure 2a DRIVER PRESSURE RECORD (SLOW COMBUSTION)

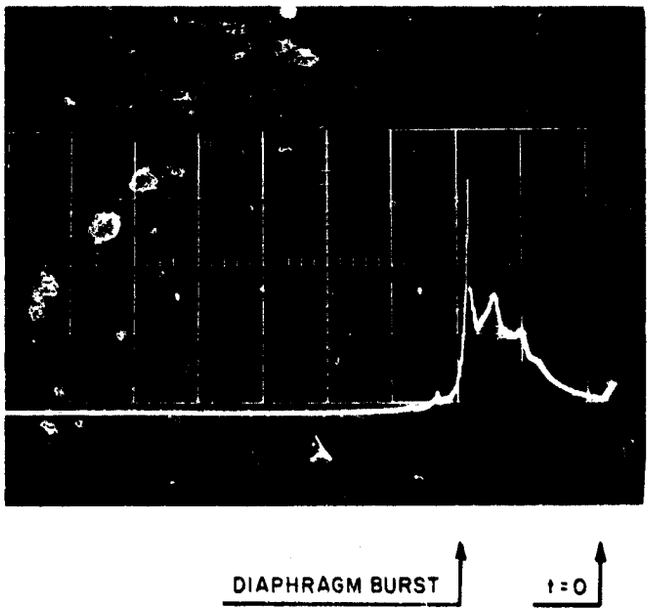

Figure 2b DRIVER PRESSURE RECORD (FAST COMBUSTION)

for photographing the event. Appropriate seals were incorporated into these ports to maintain the subatmospheric prerun pressures as well as tc contain the high transient pressures resulting when the shock wave passes. The windows are mounted flush with the inside wall of the test section to minimize distortion of the shock wave. The water inlet and outlet ports are maintained at a minimal diameter for the same reason. Plexiglass windows were used as viewing ports and were replaced frequently since the surface was severely deteriorated by the high-temperature, high-velocity gas. It was found that plexiglass had a longer life-time under these conditions than glass and also had the advantage of being con-siderably less expensive than glass. A pressure transducer was also located in the test section to monitor the pressure rise across the shock and consequently provide a double check on the shock velocity. A typical pressure record is shown in Figure 3. The slow pressure rise indicated is the result of the slow response of the pressure transducer to the step-function pressure increase.

A large expansion tank is located at the end of the tube to maintain subatmos-pheric pressure in the tube after the test. A thin Mylar diaphragm between the tube and the tank enables one to pump the tank to a much lower pressure than the tube. The primary reason for using the expansion tank was to protect the droplet generator from long-duration overpressure.

The electronics used to synchronize and monitor the shock location and spark light source or flash X-ray triggering is shown schematically in Figure 4. Four gages located in the wall of the driver tube (see Figure 1) were used to record the speed of the shock wave. The first gage was used to trigger an oscilloscope having a rastered sweep. Its output as well as the outputs of the subsequent gages were displayed on the scope trace. The trigger output of the last speed gage, located 7 inches from the droplet stream, was used to trigger the spark gap. A delay generator was used to control the time after intercept at which the trigger occurred. The output of the spark was also fed into the oscilloscope in order to monitor the precise location of the shock when the photograph was taken. A typical speed record is shown in Figure 5a and the corresponding velocity profile and shock location graph in Figure 5b. In this shot the test speed was 12,420 ft/sec.

Two types of gages were used to monitor the shock velocity: thin-film heat gages for the Mach 3 tests and ionization gages for the Mach 6 to 12 tests. The heat gages consist of a narrow strip of platinum painted on the surface of a Pyrex disk which was mounted flush with the wall of the driven tube. The change in temperature resulting from the passage of the shock was sensed and recorded. The fragility of this gage renders it impractical for the high-speed test; conse-quently, ionization gages were used for the Mach 6 to 12 tests. This gage is essentially a modified 14 mm spark plug mounted flush with the driven tube wall. The gage acts as the open end of a make-circuit which is closed by the arrival of the ionized shock layer. The ionization gage is very rugged and needs only an occasional cleaning; however, it is too insensitive to be used for the low Mach number tests.

The droplet generator system was based on a technique used by Dabora[1], in which water is forced into a cavity (void of air bubbles) and out through a capillary as shown in Figure 6. (A photograph of the drop generator appears in Figure 1b.) Unlike the Dabora system, however, this system was designed to operate in vacuum and under very high transient pressure loading (up to 700 psia). A heavy-duty

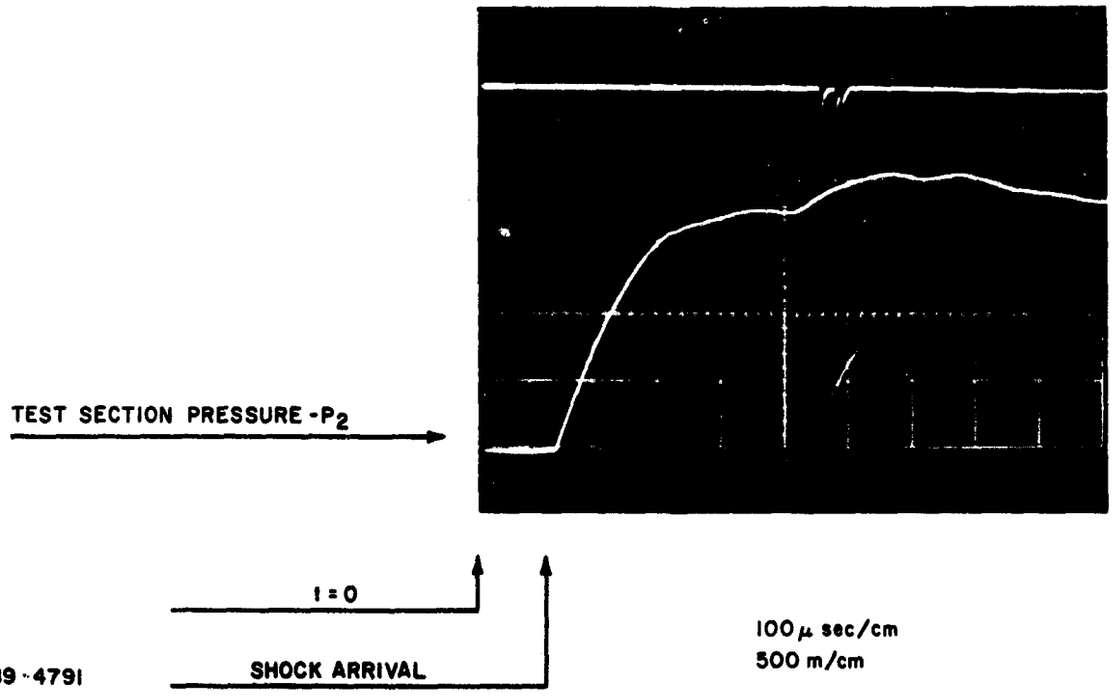

Figure 3 TEST SECTION PRESSURE RECORD

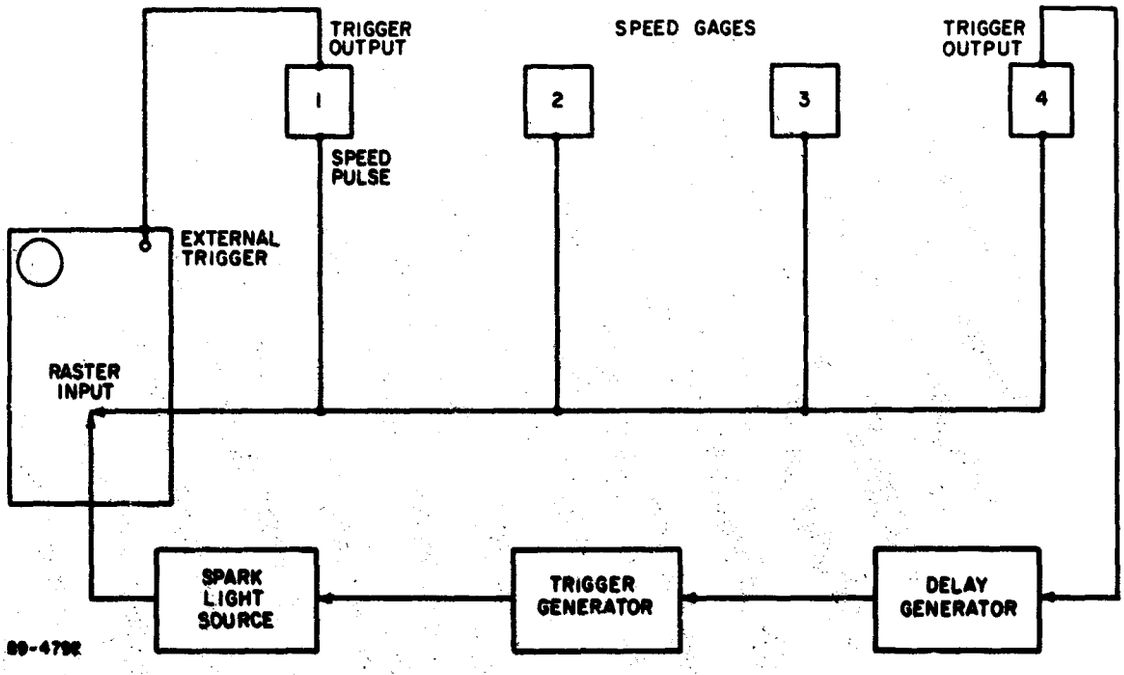

Figure 4 SCHEMATIC OF ELECTRONICS

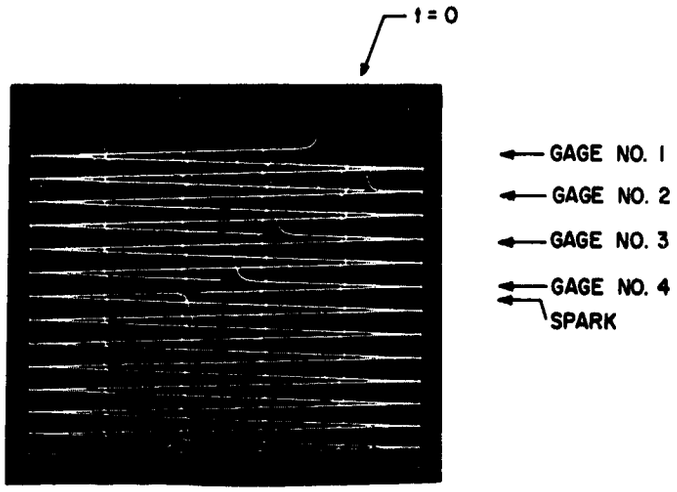

10 μ sec / MARKER

89-4793

Figure 5a SHOCK SPEED RECORD

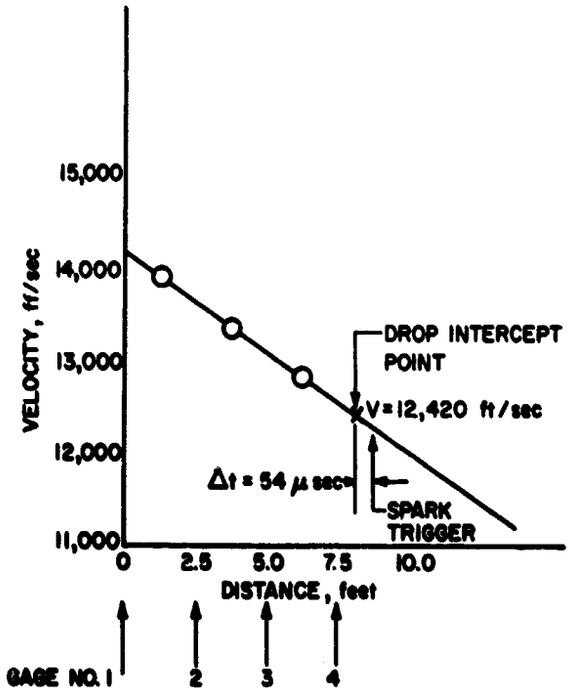

Figure 5b SHOCK TRAJECTORY

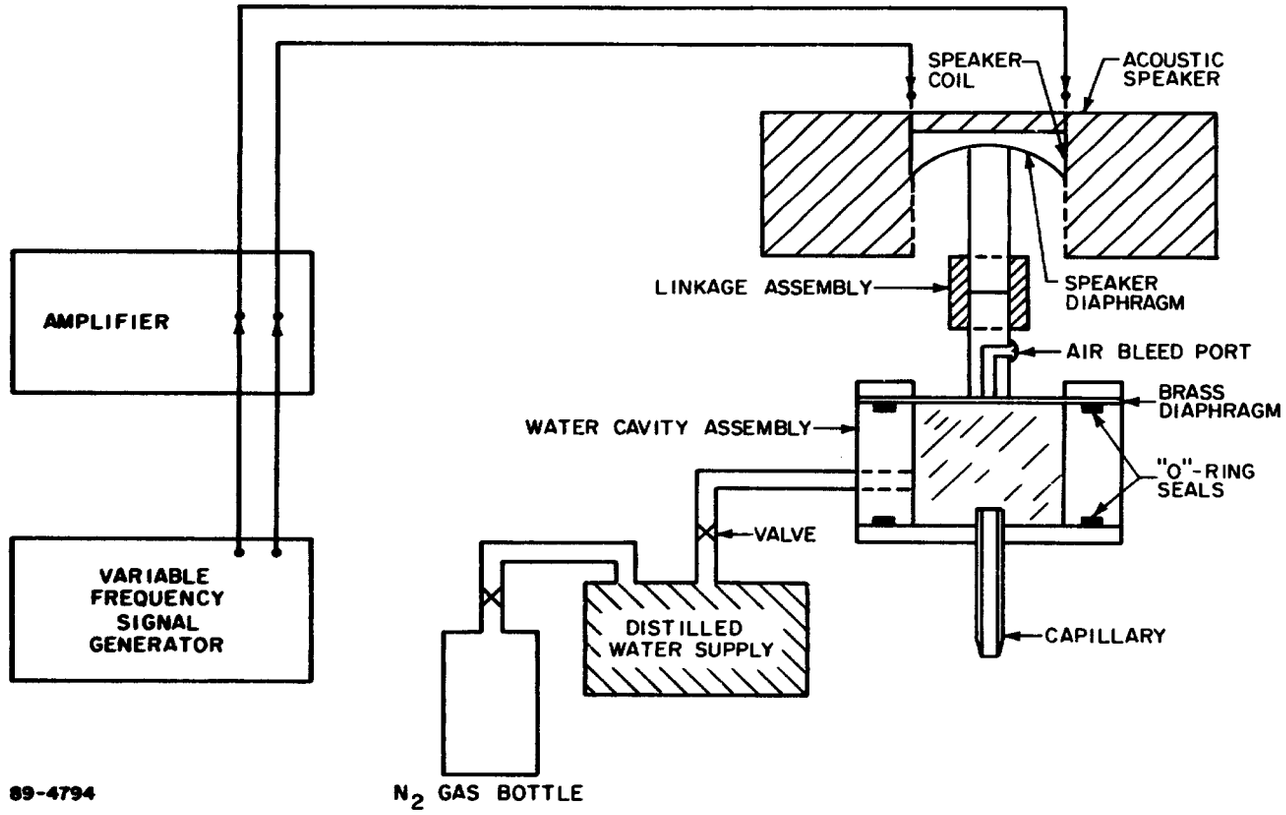

Figure 6 SCHEMATIC OF DROP GENERATOR

acoustic speaker driven by an amplified, variable frequency, sinusoidal signal was used to vibrate a 3-mil-thick brass diaphragm located at the top of the water chamber. The linkage between the speaker and the brass diaphragm was attained by cementing a Micarta rod to the speaker diaphragm and coupling it to a copper rod, soft-soldered to the brass diaphragm. An air-bleed hole was drilled through the copper rod to allow the purging of the chamber of air after each test. The capillary was epoxy adhesive-bonded into the end of the water chamber opposite the diaphragm. The cavity assembly was clamped together with three 1/4-20 bolts which compressed the two O-ring seals at each end of the droplet generator. Distilled water was driven into the chamber using nitrogen gas pressure as shown in Figure 6. The water flow into the chamber was controlled by a manually adjusted micrometer valve. The flow rate used for all capillary sizes was that rate which was adequate to maintain a chamber back pressure sufficient to establish a laminar water jet at the orifice of the capillary. Three capillary sizes were used (0.007-, 0.018-, and 0.060-inch I.D.) for three drop nominal diameters, 0.5, 1.0, and 2.1 mm, respectively. The critical frequency at which the brass diaphragm must be vibrated to sustain a stream of droplets having uniform size, spacing, and shape was determined experimentally for each capillary. The droplet stream was collected in a flask attached to the underside of the test section which was drained after each test.

Two optical systems were used during the course of the tests, namely, a single-frame spark shadowgraph and a single-frame flash X-radiograph. The former optical system is shown schematically in Figure 7a. A spark light source having an effective duration of 0.3 μsec is used to backlight the event. The light emitted by the spark gap is collimated by an f/2.5 aero-ektar lens prior to passing through the object plane. The parallel beam of light is subsequently passed through the objective lens, which serves a twofold function. First, it focusses the droplets on the film plane, and second, it images the spark gap on the camera iris which is closed down to its smallest opening. This restricting aperture limits the amount of stray radiation (primarily from the luminous air behind the shock) that can strike and thereby fog the film. A further reduction in the fog level was achieved by introducing an interference filter (4220 A) between the camera and the objective lens. The bandpass of the filter was selected to pass the radiation from the spark while rejecting the radiation from the heated air.

A Fexitron flash X-ray system utilizing a model 524 X-ray tube operating at a voltage of 105 kv was used in the X-radiograph system as shown in Figure 7b. The effective source size is less than 1 mm and has a duration of 30 nsec. A diverging beam of X-rays is emitted by the X-ray source which passes through the test section onto the film, located as close to the object plane as possible. Polaroid X-ray film, type TLX, was used because of its fine grain and high sensitivity (speed). The magnification of the object is determined by the ratio of the source-object distance to the source-film distance.

Resolution of 2 mm-diameter water droplets with the above system could not be attained without the addition of a lead salt to the water. Adequate increase in X-ray absorption was obtained by dissolving lead acetate trihydrate to the point of saturation. This solution was carefully filtered to remove undissolved material and stored in a sealed container to prevent evaporation of liquid and subsequent precipitation of solute. The effect of doping the water with lead acetate was to increase the density, viscosity, and surface tension of the

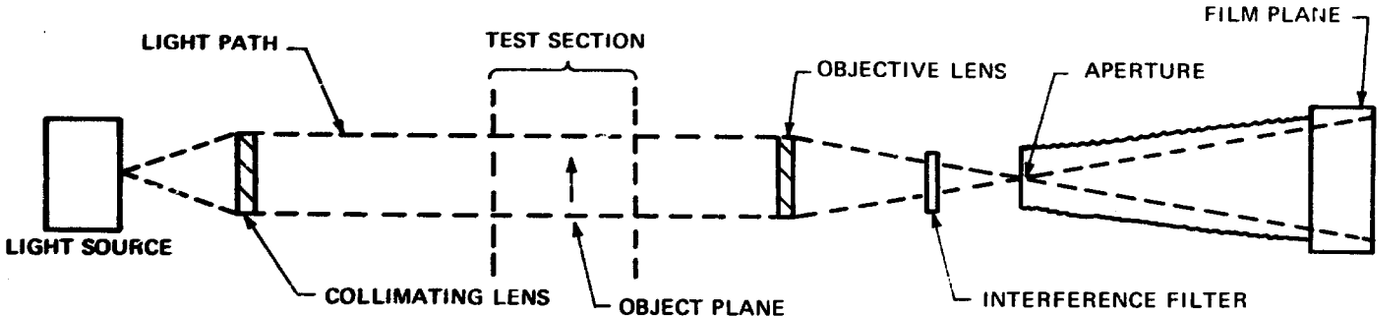

Figure 7a SCHEMATIC OF SPARK SHADOWGRAPH SYSTEM

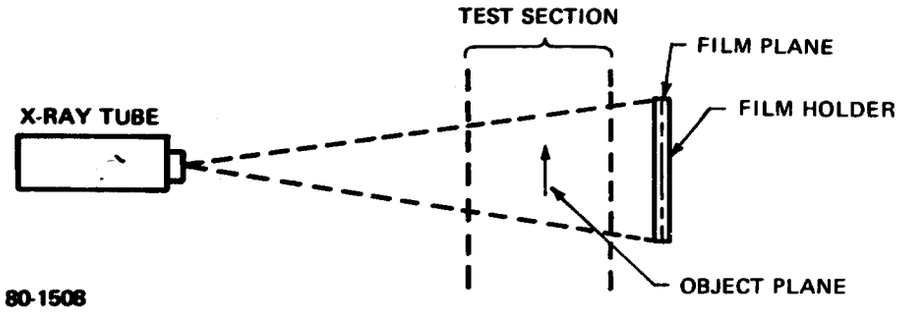

Figure 7b SCHEMATIC OF FLASH X-RAY SYSTEM

solution above those for pure water. Specifically the ratios of the density, viscosity, and surface tension of the solution to pure water values are 1.44, 1.82, and 1.05 respectively. As will be seen later, proper non-dimensionalization of the experimental results renders the data obtained with the doped water directly comparable to data obtained using pure water.

A schematic view of the drop shattering experiment in room fixed coordinates is shown in Figure 8. A drop of initial diameter and density, D_o and ρ_L respectively, is shown prior to the passage of a shock moving with a speed u_s into an initial pressure p. Gas conditions behind the shock are indicated by subscript 2. Time is measured starting from the instant the shock crosses the drop. The distance x is the coordinate of the drop relative to its initial location, and unsubscripted u is the drop speed, dx/dt.

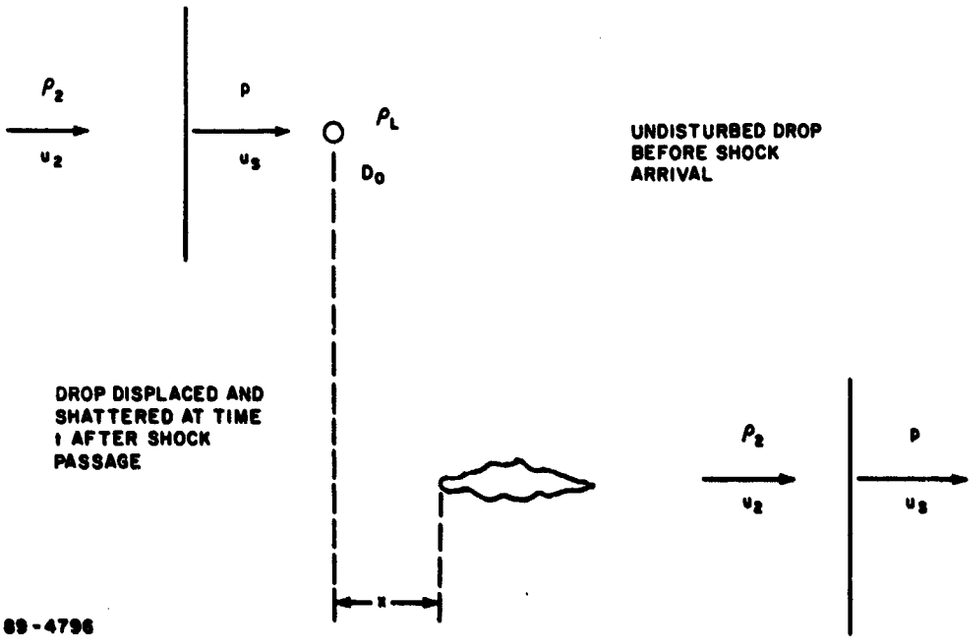

Figure 8 SCHEMATIC OF EXPERIMENT

2.2 SPARK SHADOWGRAPH DATA

Spark shadowgraph data were obtained for three reasons: First, we wished to determine accurately the distortion history of the water drops at times immediately after shock passage. These data were necessary to substantiate the first step in the theoretical analysis of drop behavior. Second, it was necessary to show that the doped drops behaved the same as the undoped drops in properly non-dimensionalized time. Finally, the spark shadowgraphs provided a simpler method than X rays to obtain an approximate idea of when the drops were shattered under the most severe test condition, $M_s = 11$, $p = 141$ torr. Studies already reported indicated approximately what the time to breakup was under low Mach number test conditions.[2,3,4]

Immediately after passage of the shock wave over the drop, the flow over the drop sets up a pressure differential between the drop's stagnation point (or pole) and its shoulder (or equator). In response to this pressure difference the drop expands normal to the flow direction and contracts in the direction parallel to the flow direction. This shape change is illustrated in Figures 9a through 13a. These shadowgraphs were obtained for distilled water drops with a 1.03 mm initial diameter overtaken by a Mach 6 shock at an initial pressure of 350 torr. Figure 9a shows a drop prior to shock arrival, while the subsequent shadowgraphs correspond respectively to times after shock passage of approximately 4, 9, 15, and 25 μsec.

Ranger and Nicholls[4] have reported that for their data at shock Mach numbers below 4, the drop distortion r/r_o (where r is the radius of the drop at its equator) could be correlated against a dimensionless time after shock passage given by $T = tu_2 b^{1/2} / D_o$ where $b = \rho_2 / \rho_L$.

To obtain accurate, general early-time distortion histories, data were acquired in the present tests over the entire experimental range; i.e., for M_s from 3 to 11, D_o from 0.5 to 2.5 mm, p from 760 to 141 torr, and doped or undoped. The results are shown in Figure 14, where r/r_o is plotted against dimensionless time T.

Since the time scale, $D_o / u_2 b^{1/2}$, varies by a factor of 10 in these experiments, Figure 14 indicates that T is the appropriate dimensionless time, and also indicates that $r(T)/r_o$ is concave upward at early time. The significance of these data with regard to the analysis will be discussed later.

Similar results for one test condition, but for later time are shown in Figure 15. Here distortion data for drops saturated with lead acetate are compared, in dimensionless time, against results obtained by Reinecke and McKay[5] at the same test condition (M=6). Figure 15, along with the two doped points in Figure 14, indicates that the density difference between doped and undoped drops is adequately accounted for by the appearance of $\rho_L^{1/2}$ in T.

The spark shadowgraph system was also employed to determine the approximate time required to shatter the drops at the most severe test conditions, M_s = 11, p = 141. These tests indicate a dimensionless time to breakup, T_b, of about 3, distinctly below the values of 5 to 6 reported at Mach 2 to 3.5, also on the basis of shadowgraph data, by Ranger and Nicholls.[4]

Finally, Figure 11a indicates a spark shadowgraph of a drop at Mach 6, 30 μsec after shock passage (T = 1.28). By this time a substantial amount of water has been stripped from the equator of the drop and has entered its wake, rendering the wake opaque to visible light. Comparison of Figure 11a with the undisturbed drop shown in Figure 9a indicates that simple mass continuity precludes the possibility that the entire shadow in Figure 11a contains only water. Clearly the remaining unstripped mass of the original drop is confined to a lens-shaped volume at the front of the shadow in Figure 11a. How much water remains, however, cannot be determined from the shadowgraph. Instead, the flash X-ray system was employed to measure the remaining unstripped mass of the drop.

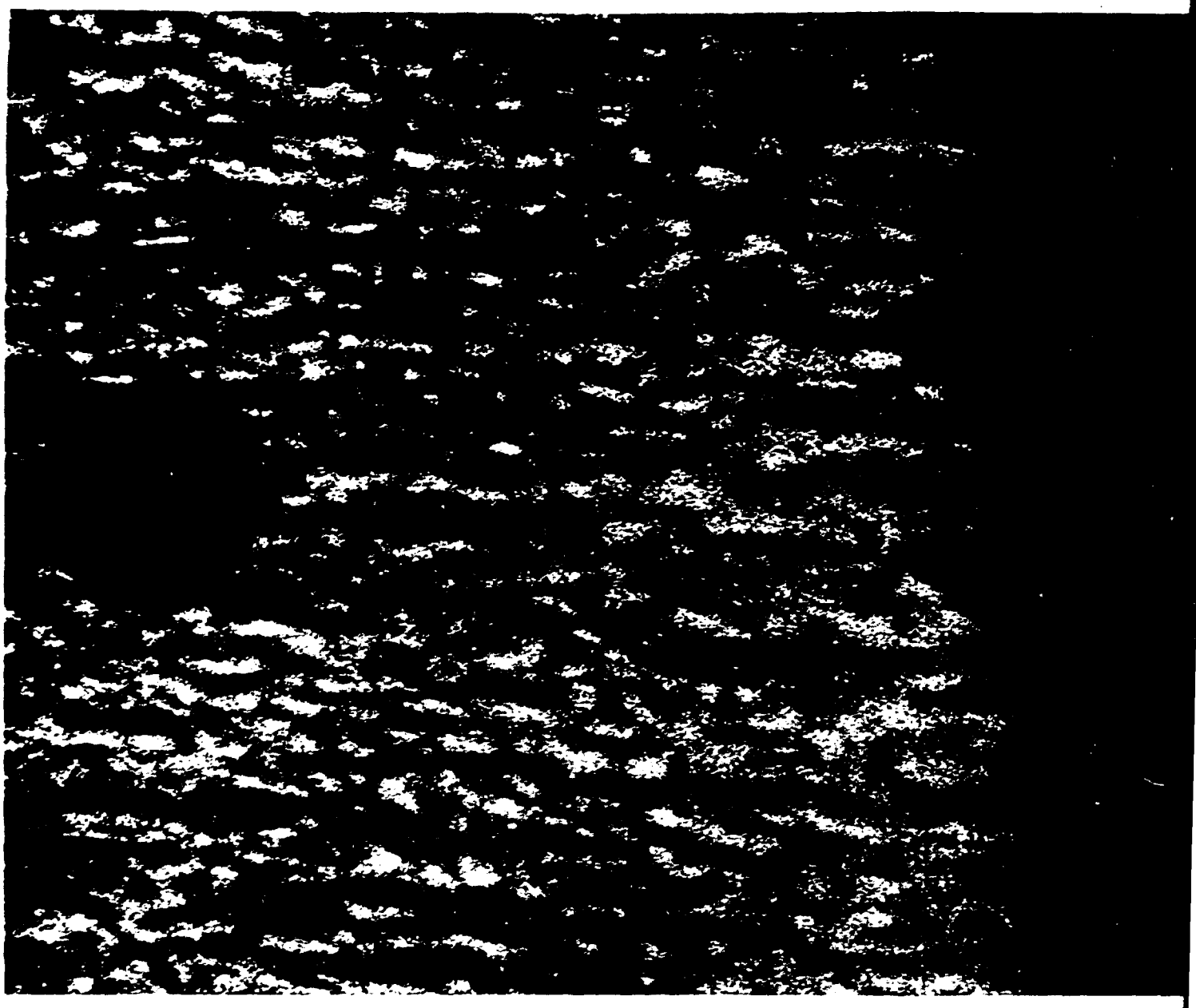

a. SHADOWGRAPH

Figure 9 UNDISTURBED DROP PRIOR TO SHOCK ARR

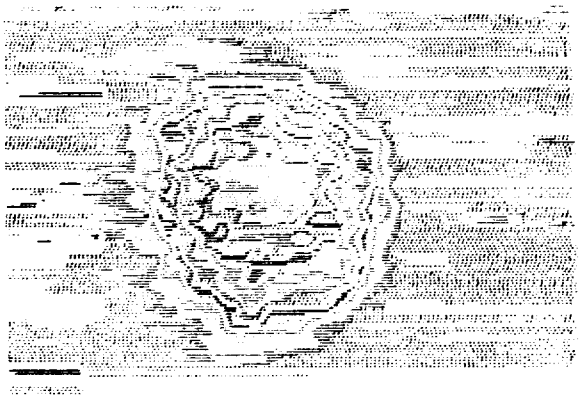

b. ISOPHOTE OF RADIOGRAM

UNDISTURBED DROP PRIOR TO SHOCK ARRIVAL

2

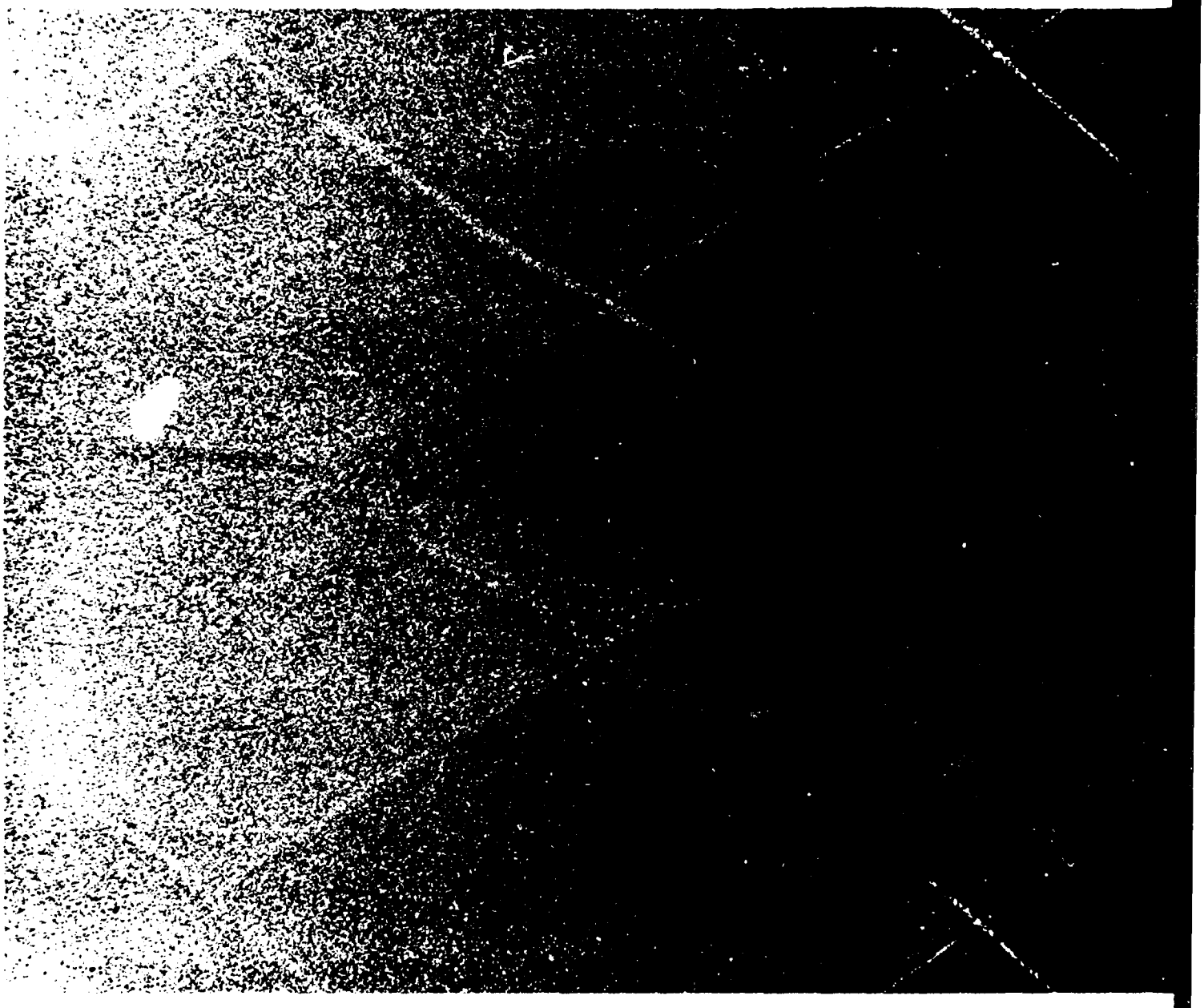

a. SHADOWGRAPH

Figure 10 DROP AFTER SHOCK PASSAGE; $M_s = 6$, p_1 = 350 torr, T

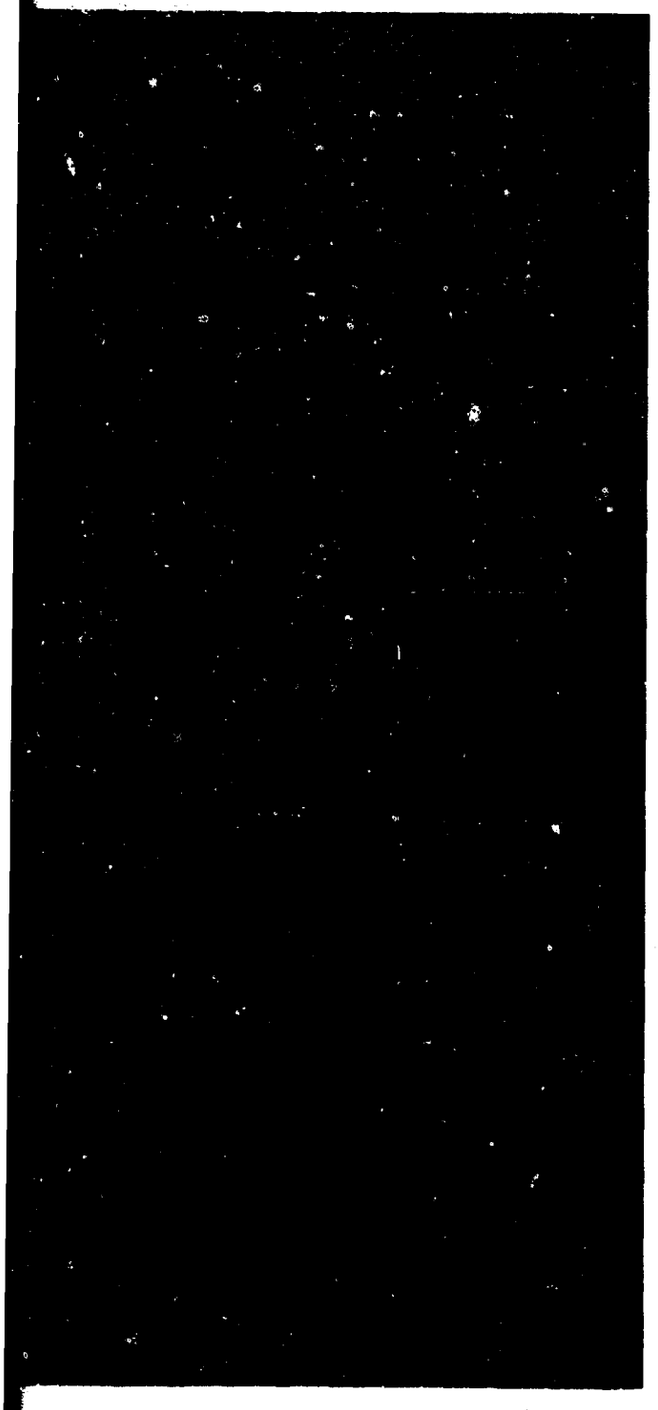

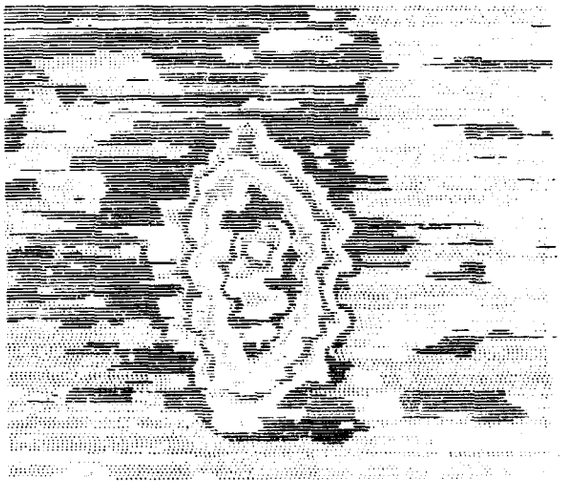

h. ISOPHOTE OF RADIOGRAM

AFTER SHOCK PASSAGE; M = 6, p_∞ = 350 torr, T 0.3

2

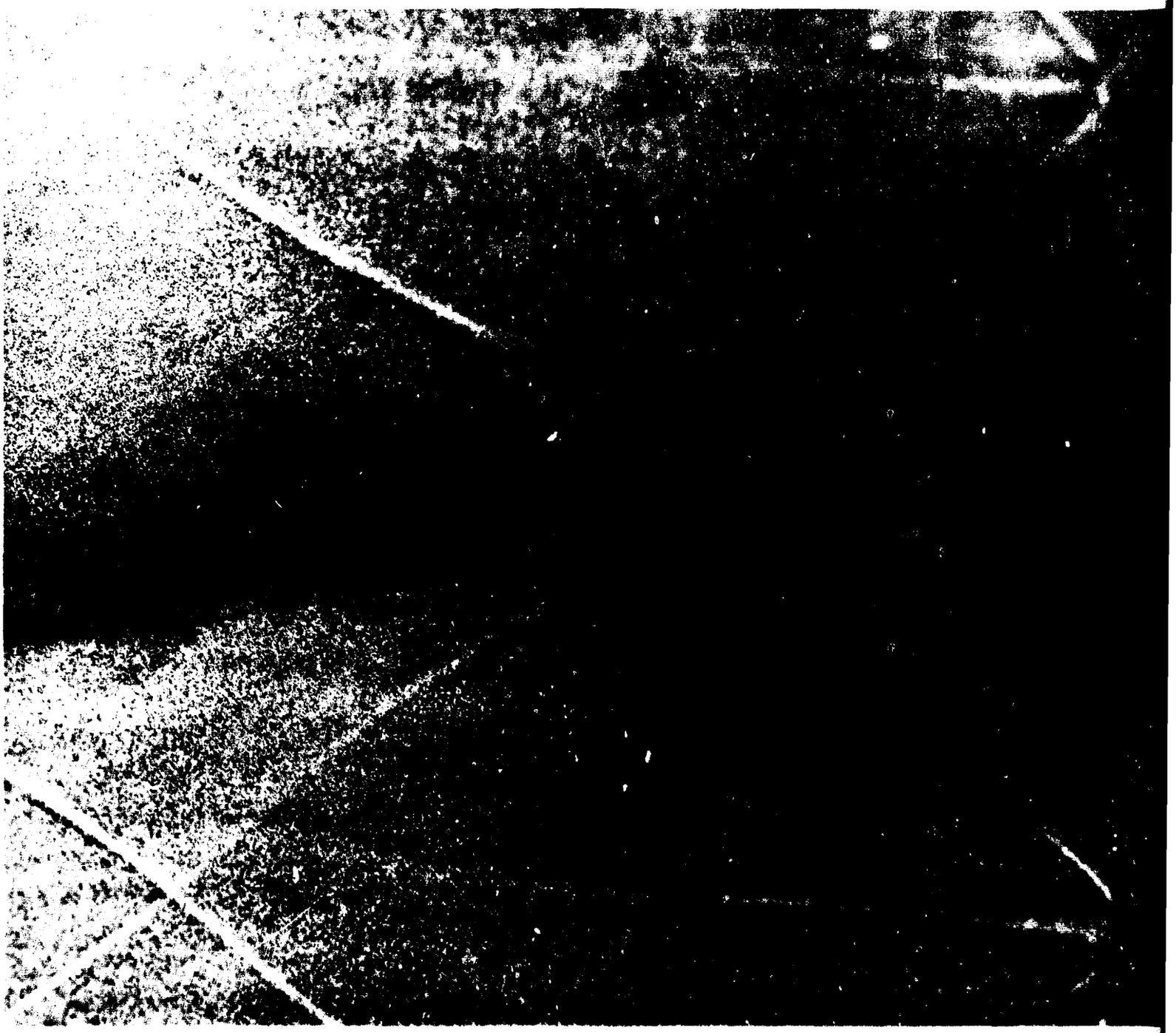

a. SHADOWGRAPH

1

Figure 12. DROP AFTER SHOCK PASSAGE; M = 6.5, 350

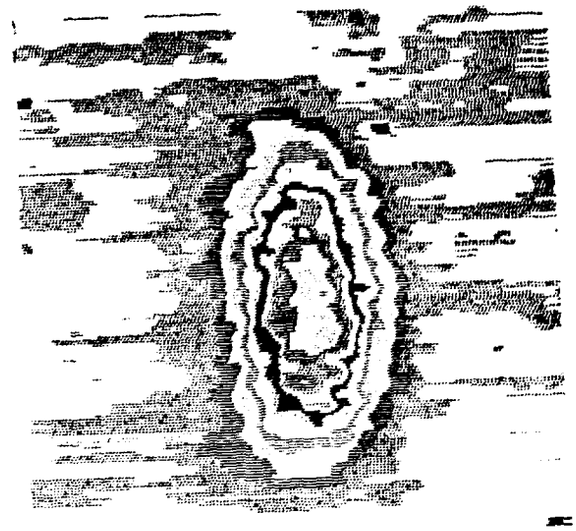

b. ISOPHOTE OF RADIOGRAM

FTER SHOCK PASSAGE; M = 6, p_∞ = 350 torr, T· 0.8

2

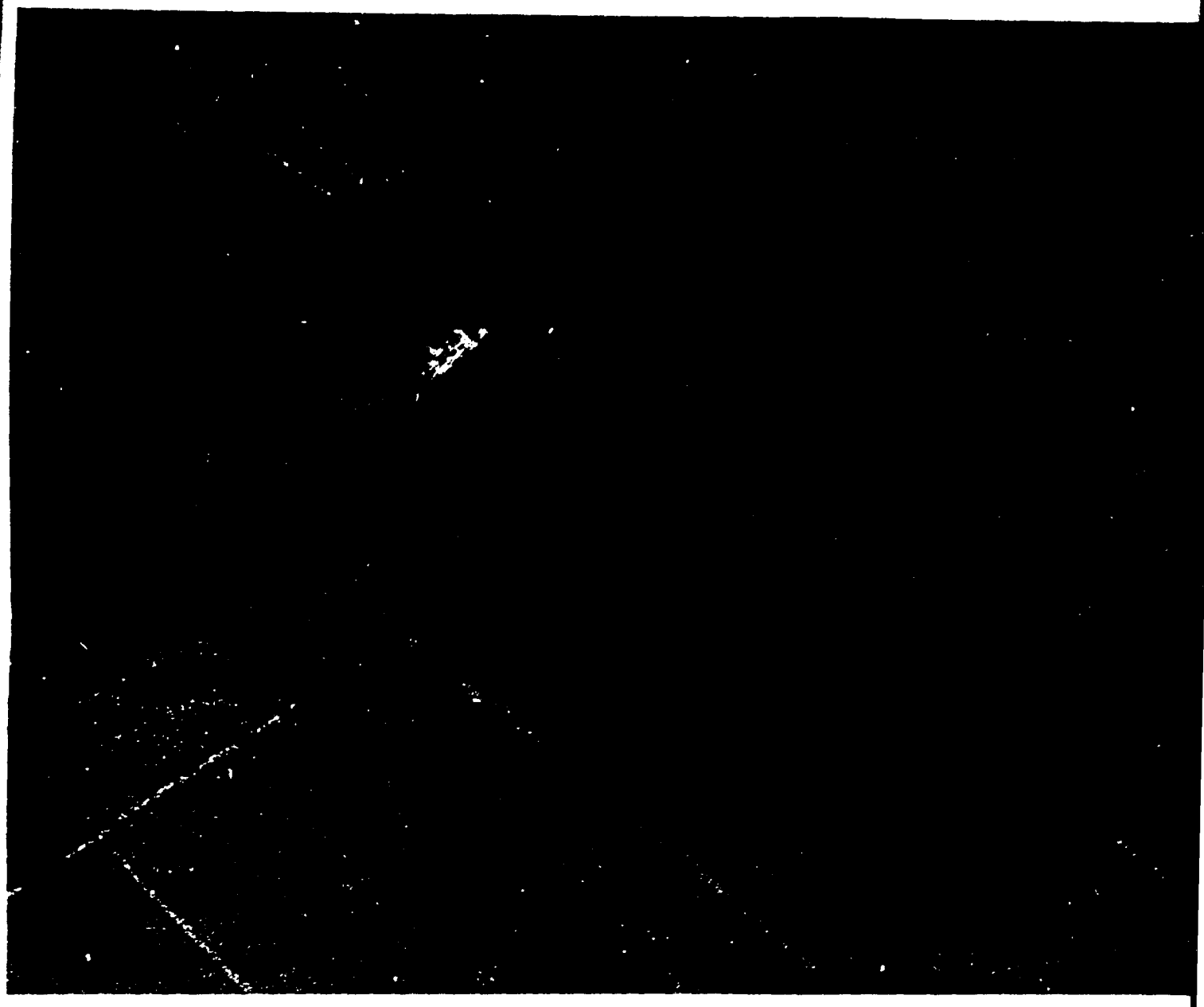

a. SHADOWGRAPH

Figure 12 DROP AFTER SHOCK PASSAGE; M 6, p 350 torr, T 1

b. ISOPHOTE OF RADIOGRAM

H

ROP AFTER SHOCK PASSAGE; $M = 6$, $p_\infty = 350$ torr, γ 1.3

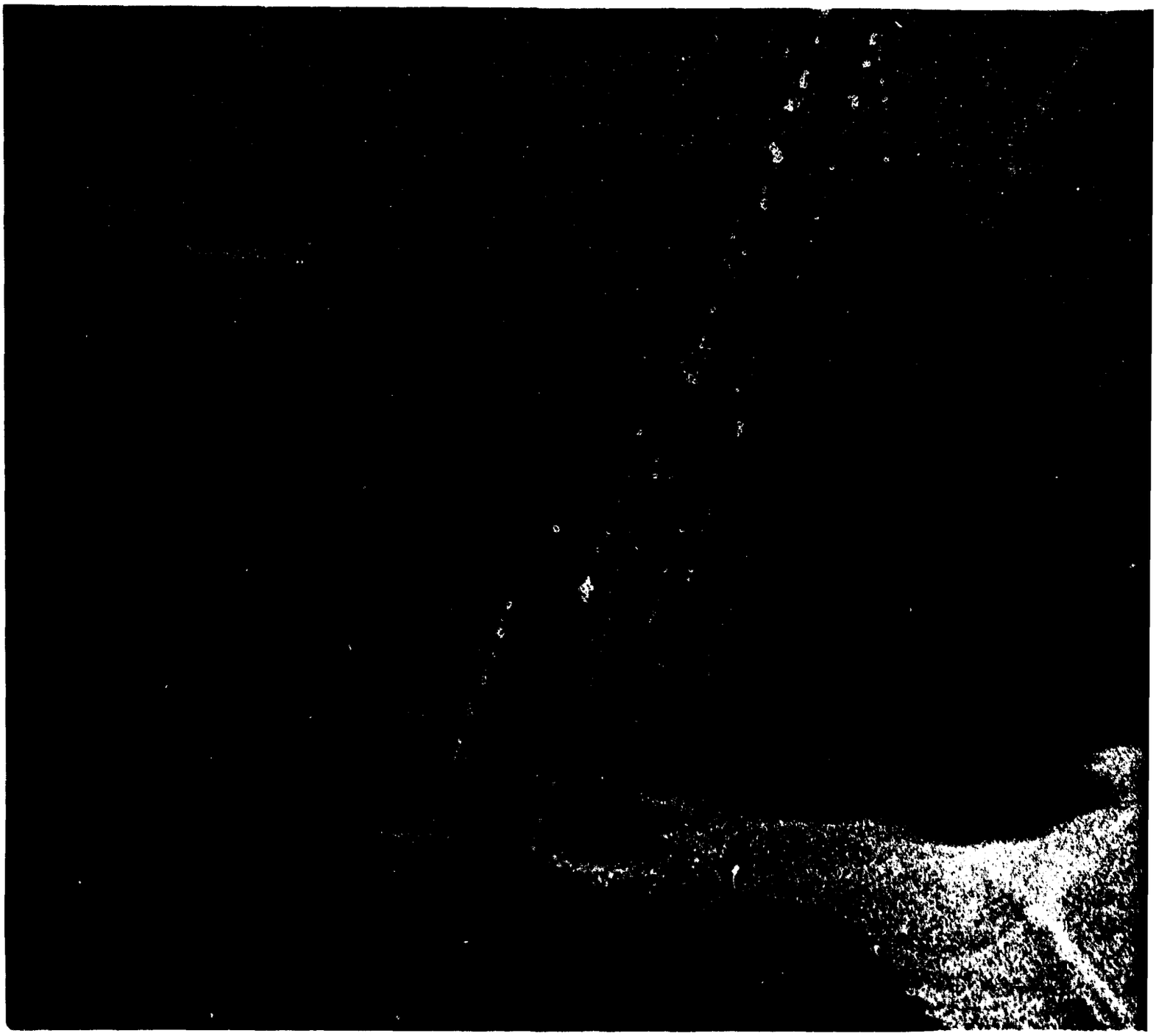

a. SHADOWGRAPH

Figure 13 DROP AFTER SHOCK PASSAGE; $M_s = 6$, P_o = 350

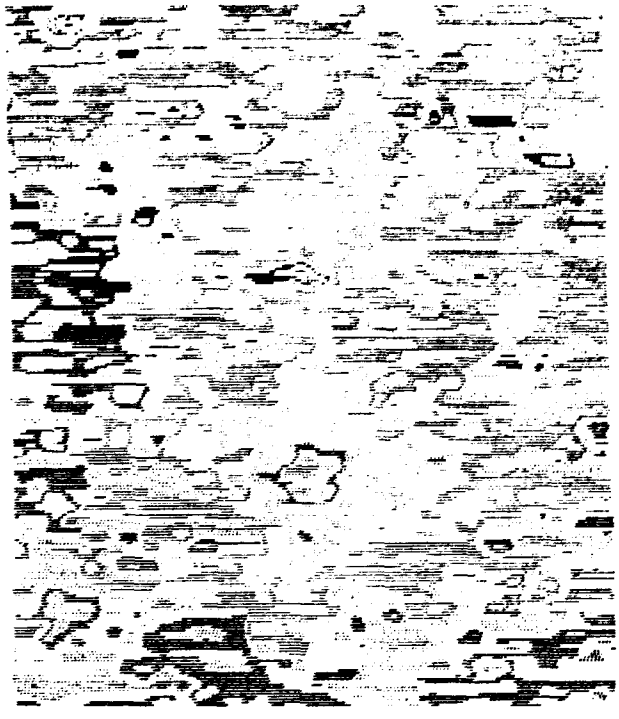

b. ISOPHOTE OF RADIOGRAM

ROP AFTER SHOCK PASSAGE; M = 6, p_{∞} = 350 torr, T 2.1

2

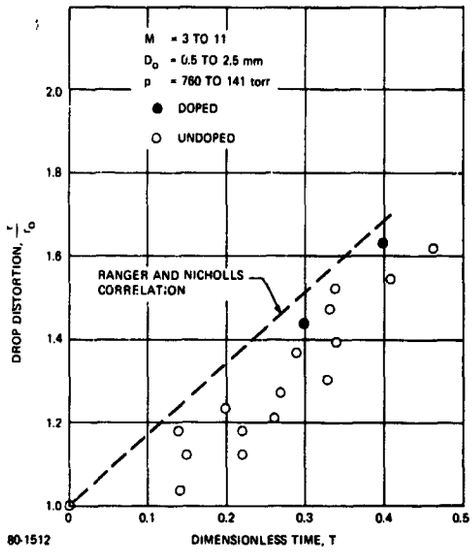

Figure 14 EARLY-TIME DROP DISTORTION HISTORY

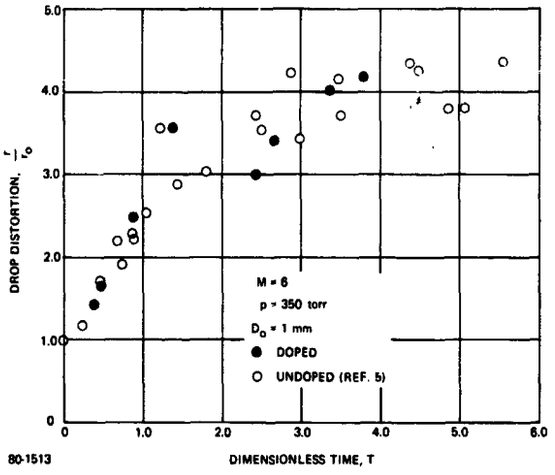

Figure 15 A COMPARISON OF DROP DISTORTION HISTORIES FOR DOPED AND UNDOPED DROPS

2.3 X-RADIOGRAM DATA

Where a pulse of X-rays traverses a homogeneous, partially X-ray-transparent body, the ratio of transmitted-to-incident X rays or photons is proportional to $e^{-C_1 z}$, where z is the local thickness of the body along the X-ray path. Moreover, in the "linear" response region of an X-ray plate, the photographic density is proportional to the logarithm of the flux or number of photons striking the film. Combining these relations immediately shows that the density of the X-ray plate is given by $C_1 + C_2 z$, where C_1 is simply the background density of the film, i.e., where $z_1 = 0$. Thus, if the path length z is known at any point corresponding to the X-ray image, C_2 can be calculated and the path length elsewhere can be computed from the local relative film density. Even if the film response is not strictly linear, the relation between film density and path length can be obtained experimentally from the X radiogram of a body of known, varying thickness.

Now consider a drop of water containing a lead salt in solution. X rays traversing the drop will be absorbed by the lead ions. Assuming that the X rays are uniformly dispersed in the water, the film density in the resulting radiogram will be proportional to the amount of water along the X-ray path. Then a scanning microdensitometer may be used to measure the distribution of film density over the drop image in the X-ray plate by plotting lines of constant film density and the drop mass or volume obtained from these "isophote" diagrams by integration, in the same manner that the volume of a mountain may be calculated from a contour map.

This method was employed to measure the mass remaining in liquid drops as a function of time after shock passage. The scanning microdensitometer isophote of a doped, spherical, 2.12-mm-diameter, undisturbed water drop is shown in Figure 9b. The slight apparent oblateness of the drop is due, not to real non-sphericity, but to a slightly different magnifications in the vertical and horizontal scan of the microdensitometer. The increasing film density and corresponding sphere secant is indicated in the isophote by the digitized, nine-unit color code of dotted red, solid red, white, dotted blue, solid blue, white, dotted green, solid green, and white. The film density versus water path length calibration obtained from this, and a similar isophote, is shown in Figure 16. The calibration points were obtained by scanning along orthogonal diameters on each of two different radiograph of different drops. Thus the data represent four scans. Although it is not apparent on the distorted scale of Figure 16, the calibration indicated a nearly linear X-ray plate response except near the image edges where the finite size of the microdensitometer aperture distorted the calibration. To check the repeatability of film responses from plate to plate, of the drop diameter, of the film and densitometer magnification, etc., the calibration was used to calculate the volume of an undisturbed drop X-rayed late in the test program. The mass of the drop was computed to be 0.93 of the calibration drop, indicating a very satisfactory level of overall repeatability. The integrations to obtain drop mass were carried out on an IBM 360 computer using as input a tape of the microdensitometer output corresponding to the isophotes and digitized over 64 shades of intensity.

Typical isophotes of doped, X-rayed drops at various times after shock passage are shown in Figures 10b through 13b and correspond in dimensionless time, T, to the respective shadowgraphs. The aerodynamics parameters were the same in these X-ray tests as is illustrated in Figures 10a through 13a; i.e., Mach 6 at 350 torr. However, the initial drop diameter for the X-ray tests was 2.12 mm (this diameter yielded significantly better X-ray resolution than 1 mm drops), and the water was saturated with lead acetate, which increased the density, viscosity, and surface tension. As expected, Figures 10, 11, and 12 indicate that the remaining unstripped water is confined to a lenticular volume at the front of the shadowgraph image and that the stripped mass is very tenuously distributed. Figure 13 shows the drop at a fairly late state of disintegration. In this particular test it has broken into two smaller drops. The shadowgraph in Figure 13a was chosen from several available, because it was geometrically compatible with the isophote. The drop separation into two distinct droplets was not generally seen in the tests. In fact, as will be discussed later, the final disintegration process results in a random and unpredictable geometry.

From such isophotes, the drop mass histories shown in Figures 17, 18, and 19 were obtained. At the Mach 3 condition (see Figure 17), the drop mass decreases smoothly, and indicates a time to breakup of about 150 μsec. At Mach 6 (see Figure 18), the drop mass decreases smoothly to about 40 percent of its initial value, at which time (about 50 microseconds) the mass decreases abruptly.

In the Mach 11 case (see Figure 19) the drop image on the X-ray plates abruptly dropped below the background density after about 25 μsec. Several attempts were made to obtain X-ray images at about 25 μsec. These tests apparently yielded either dark X-ray plates or images whose computed mass exceeded 70 percent of the original mass. Those points showing either 70 percent or more or a dark plate may be seen in Figure 19. This result is apparently caused by an extremely abrupt, catastrophic disintegration of the drop at about 25 μsec after shock passage.

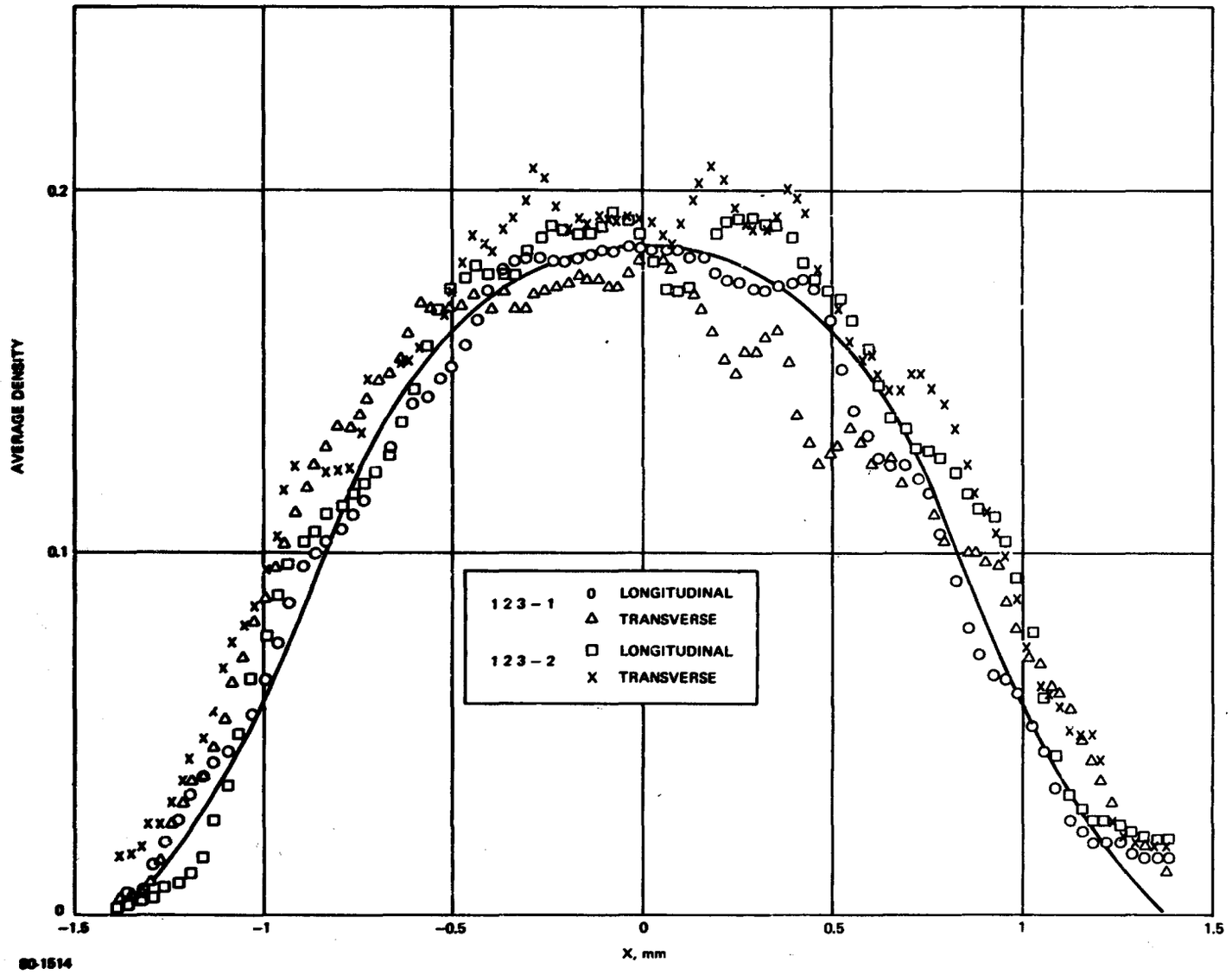

Figure 16 X-RAY PLATE CALIBRATION

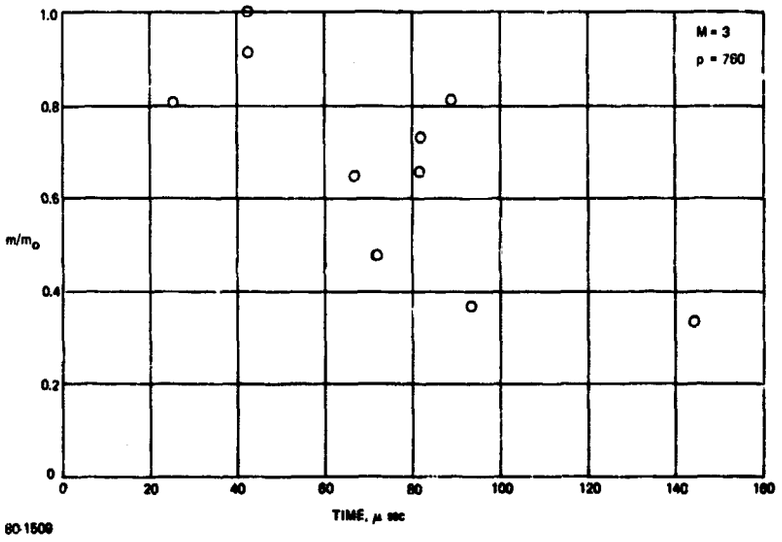

Figure 17 DROP MASS HISTORY; M = 3, p = 760

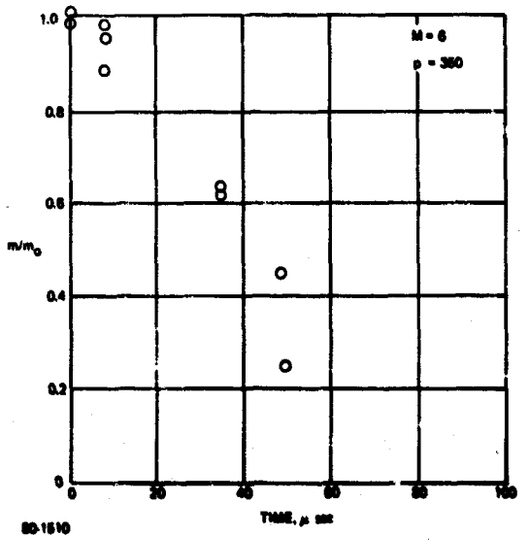

Figure 18 DROP MASS HISTORY; M = 6, p = 350

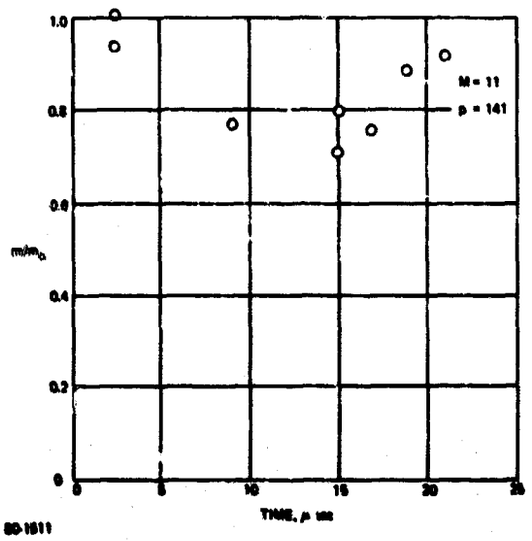

Figure 19 DROP MASS HISTORY; M = 11, p = 141

3.0 CORRELATION AND INTERPRETATION OF EXPERIMENTAL DATA

The experimental data reported in Section 2.0 has been correlated in terms of appropriate nondimensional parameters. The following material describes the derivation of the nondimensional parameters from theoretical considerations and the correlation of the data.

3.1 EXPERIMENTAL DROP TRAJECTORIES

We will here simply cite results already reported in the literature.[5] The trajectory of a drop is strongly affected by the deformation of the drop, which is caused by the suddenly imposed pressure differential between the equator and the poles. This deformation changes the drag coefficient of the drop, and the drop trajectory becomes difficult to compute. The stripping of mass from the drop is also coupled to the trajectory computation. Under such circumstances it becomes simpler to determine the drop trajectory experimentally.

The trajectory of a deforming drop may be correlated in terms of a dimensionless time based on the time constant of the deformation. The magnitude of the pressure differential is given by the dynamic pressure $1/2\ \rho_2 u_2^2$ acting on the drop. Dimensional analysis shows that the characteristic time associated with deforming the drop by an amount on the order of the original diameter, D_o, in some direction is given by

$$t^* = \frac{D_o}{u_2}\sqrt{\frac{\rho_L}{\rho_2}} \qquad (1)$$

Hence we can define a nondimensionalized time, T, by the equation

$$T = \frac{t}{t^*} = \frac{t\,u_2}{D_o}\sqrt{\frac{\rho_2}{\rho_L}} \qquad (2)$$

Let $X = x/D_o$ be the distance in original drop diameters that the drop has moved in the shock tube at time t. The drop trajectory data compiled at Avco can be correlated by the relationship[5]

$$X = 0.8\,T^2, \qquad (3)$$

which corresponds to a constant acceleration trajectory with an average drag coefficient of about 2.1.

3.2 DROP DEFORMATION

The complete analysis of the deformation of a waterdrop following the passage of a shock wave is a formidable problem far beyond the scope of the present study. Instead of attempting a complete numerical or analytical solution to the equations of motion for the drop, we have explored two approximate analyses in order to gain some insight into the general character of the deformation and the governing parameters.

In the first approach, the initial deformation of the drop was considered. Provided attention is confined to the period immediately following the shock passage (the possible length of such a period will be explored subsequently), the boundary of the drop may be approximated as the initial sphere, and the solution to the equations of motion can be developed in spherical harmonics. Let ϕ be the velocity potential for the motion, satisfying the Laplace equation in spherical coordinates

$$\Delta^2 \phi = \sin\theta \frac{\partial}{\partial r}\left(r^2 \frac{\partial \phi}{\partial r}\right) + \frac{\partial}{\partial \theta}\left(\sin\theta \frac{\partial \phi}{\partial \theta}\right) = 0 , \tag{4}$$

where r is the radial coordinate and θ is the azimuth angle measured from the pole of the drop (i.e., the axis of symmetry of the flow).

The general solution to Equation (4) is

$$\phi = \sum_n A_n(t)\, r^n P_n(\theta) , \tag{5}$$

where P_n are the Legendre polynomials in $\mu = \cos\theta$:

$$P_o = 1, P_1 = \mu , P_2 = \frac{1}{2}(3\mu^2 - 1), P_3 = \frac{1}{2}(5\mu^3 - 3\mu), \ldots .$$

It can be shown that an impulsive pressure $\tilde{\omega}$ is related to an imposed value of ϕ on the boundary of the drop by the equation $\phi = \tilde{\omega}/\rho_L$ + constant, where ρ_L is the water density. Since in our case the "impulsive pressure" is actually applied continuously, we have $\tilde{\omega} = pt$. In addition, the arbitrary constant just referred to can be taken to vanish without loss of generality. We then have at the surface of the drop $r = r_o$

$$\phi = \Sigma\, A_n(t)\, r_o^n\, P_n(\theta) = \frac{pt}{\rho_L} , \tag{6}$$

which is sufficient to determine the coefficients A_n for a given pressure distribution.

This approach has been taken by Burgers (referenced in Engel[2]) in the case of a symmetrical pressure distribution of the form

$$p = p_e + (p_s - p_e)\cos^2\theta \tag{7}$$

such as would be obtained in subsonic inviscid flow. He then obtains

$$A_0 = \frac{1}{3} \frac{P_s + 2P_e}{\rho_L} t ,$$

$$A_2 = \frac{2}{3} \frac{P_s - P_e}{\rho_L} \frac{t}{r_o^2} , \tag{8}$$

$$A_1 = A_3 = A_4 = A_5 = \ldots = 0 .$$

The initial deformation of the drop can be obtained from this solution by expressing the radial velocity component v in terms of the velocity potential:

$$v = \frac{dr}{dt} = - \frac{\partial \phi}{\partial r} = - \sum n A_n r^{n-1} P_n . \tag{9}$$

By integrating in time, we get the relative deformation of the contour at any point on the periphery of the drop:

$$r - r_o = - \sum n r_o^{n-1} P_n \int_o A_n \, dt . \tag{10}$$

In terms of the Burgers' solution, this displacement becomes at the poles of the drop

$$r - r_o = - \frac{2}{3} \frac{P_s - P_e}{\rho_L} \frac{t^2}{r_o} , \tag{11}$$

and at the equator of the drop

$$r - r_o = \frac{1}{3} \frac{P_s - P_e}{\rho_L} \frac{t^2}{r_o} . \tag{12}$$

In her report, Engel[2] compares Burgers' result with her experimental data on the equatorial dilatation of waterdrops. There appears to be a numerical error in Engel's computations of the Burgers' solution, however, and the apparent agreement of experiment with theory shown in her report is spurious. We have reduced Engel's data and Burgers' theory in terms of the dimensionless time

$$T = \frac{t u_2}{D_o} \sqrt{\frac{\rho_2}{\rho_L}} , \tag{13}$$

where u_2 is the initial gas velocity relative to the drop, ρ_2 is the gas density and D_o is the initial drop diameter.

Burgers' solution then becomes simply

$$\delta \equiv \frac{D}{D_o} - 1 = \frac{2}{3} C_p T^2 \tag{14}$$

for the relative equatorial dilatation, where

$$C_p = \frac{P_s - P_e}{1/2\ \rho_2 u_2^2} \tag{15}$$

The solution is plotted in Figure 20 for the subsonic incompressible value $C_p = 9/4$, and it can be seen that although the experimental data are fairly well correlated in terms of the dimensionless time, the agreement with Burgers' solution is not satisfactory.

It is worth noting that recently Ho[6] has derived much more complete solutions to the drop deformation equations, and that his solutions are in general agreement with Burgers' simplified analysis for the initial deformation assuming an inviscid pressure distribution.

In an attempt to determine the effect of the assumed pressure distribution on the analytical result, we derived the solution for the initial deformation for a case in which the pressure had the same (subsonic) variation over the windward side of the drop, but was constant over the leeward side of the drop rather than being symmetrical with respect to the equatorial plane. Such a pressure distribution should be a rough approximation to the actual distribution on a drop with a wake. Fourier-analyzing this distribution and truncating at the fourth term, we obtained

$$P = P_e + \left(\frac{P_s - P_e}{2}\right)\left(\frac{1}{2} + \frac{8}{3\pi}\cos\theta + \frac{1}{2}\cos 2\theta + \frac{8}{15\pi}\cos 3\theta\right) \tag{16}$$

to within a percent or so of the postulated distribution. Substituting in the above analysis, we determined that the corresponding equation for the dilatation of the drop equator is

$$r - r_o = \frac{1}{6}\ \frac{P_s - P_e}{\rho_L}\ \frac{t^2}{r_o}, \tag{17}$$

half the Burgers' result, and even more out of line with the experimental data.

Figure 21 shows the deformation of the drop predicted by this analysis after an arbitrary small time. It may be observed that the drop tends to flatten considerably more on the windward than on the leeward side, and that the point of maximum lateral deformation is slightly forward of the original equator. The

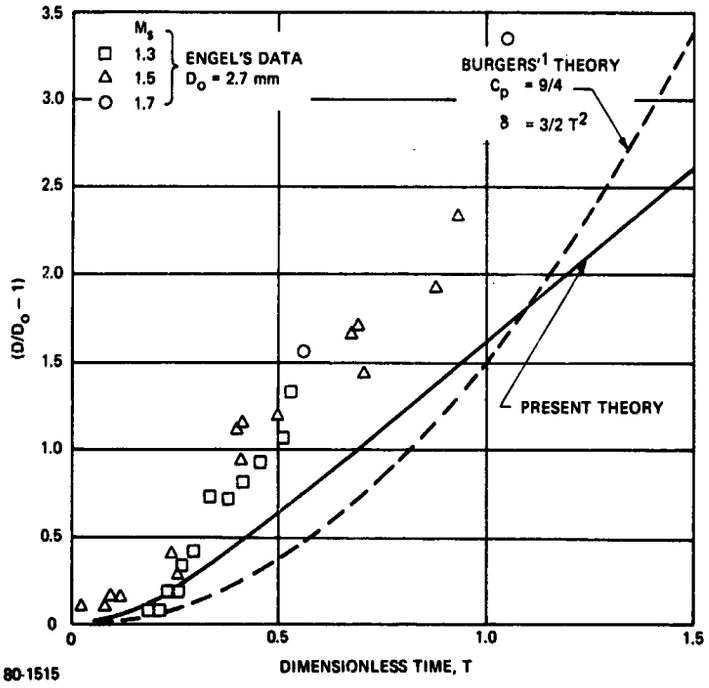

Figure 20 DROP DEFORMATION: COMPARISON OF ENGEL'S DATA AND BURGERS' SOLUTION

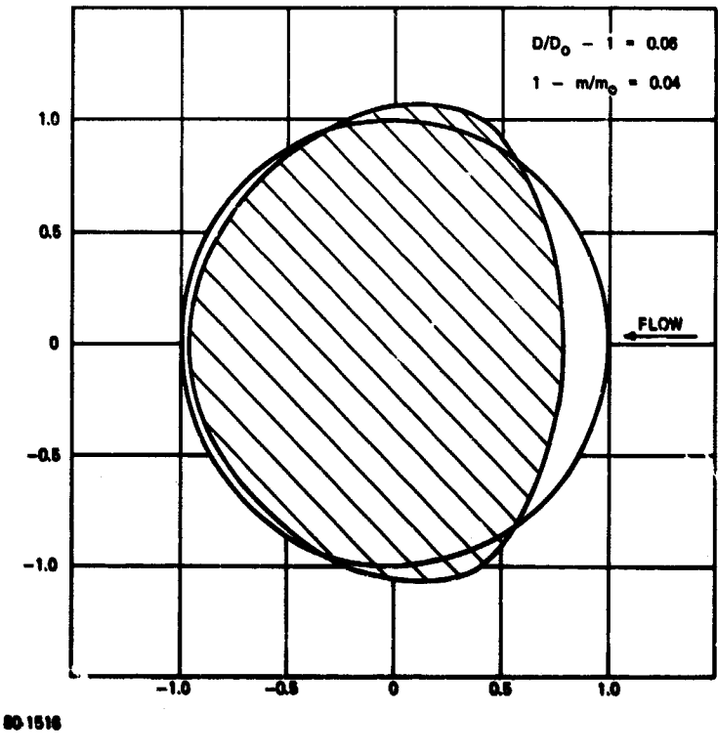

Figure 21 DROP FLATTENING WITH SIMULATED WAKE FLOW

maximum lateral dilatation is close to the dilatation at the original equator, however, and the observation just stated still holds true.

At this point, it was concluded that the analysis of the initial deformation of the drop was simply not applicable to the observed experimental behavior. The reason is probably either that the physical time scale of the observed deformation is much larger than the time scale which describes the region of validity of the analysis, or that the assumption of "impulsive pressures" is somehow invalid. In either case, the analysis is mathematically correct but physically irrelevant.

Our second approach to a solution to the deformation problem was more successful. In this approach we discarded the possibility of an exact mathematical solution, no matter how restricted the region of validity, and considered the drop to be disk-shaped rather than nearly spherical. The reason for making this assumption was that a simple approximate solution could then be obtained for all times.

Let R be the radial coordinate in a cylindrical coordinate system with axis along the axis of symmetry of the drop, and let v be the corresponding fluid velocity component in the drop. Our primary assumption is that the flow variables do not depend on the axial coordinate but are (in some approximate sense) uniform from front to back of the drop at any radius R. This assumption cannot be justified a priori, but it should be borne in mind that the purpose of this analysis is to get a rough idea of the deformation of the drop rather than a detailed solution. The radial equation of motion in the drop then becomes

$$\frac{\partial v}{\partial t} + v \frac{\partial v}{\partial R} = - \frac{1}{\rho_L} \frac{\partial p}{\partial R} . \tag{18}$$

We now integrate this equation from the axis R = 0 to the rim R = r :

$$\frac{d}{dt} \int_0^{r(t)} v dR + \frac{1}{2} v^2(r) = \frac{P_s - P_e}{\rho_L} \tag{19}$$

The outflow velocity is assumed to vary as some power of R :

$$\frac{v}{v(r)} = \left(\frac{R}{r}\right)^k \tag{20}$$

Substituting in Equation (19) and integrating, we obtain

$$\frac{r}{1+k} \frac{d^2r}{dt^2} + \frac{3+k}{2(1+k)} \left(\frac{dr}{dt}\right)^2 = \frac{P_s - P_e}{\rho_L} ,$$

or in dimensionless variables

$$\frac{1+\delta}{1+k}\,\frac{d^2\delta}{dT^2} + \frac{3+k}{2(1+k)}\left(\frac{d\delta}{dT}\right)^2 = 2C_p. \tag{21}$$

Equation (21) has been integrated numerically for various values of the exponent k. The results shown on Figure 22 demonstrate that the solution is not a very sensitive function of k , and we shall use the solution for k = 1 as the reference solution.

The main characteristics of the reference solution are that it initially follows the "transient" solution

$$\delta = 2C_p T^2 \tag{22}$$

(which incidentally is three times larger than the Burgers' solution), but that it very rapidly approaches the "steady-state" solution

$$\delta = \sqrt{2C_p}\ T + \text{const.} \tag{23}$$

Essentially the steady state is reached by T = 1/2. We may infer from this that the initial solutions discussed previously are probably invalid because their region of validity is too restricted.

The reference solution has been plotted in Figure 20, and it is seen to offer somewhat better agreement with Engel's data than with the Burgers' solution. Its agreement with the higher-speed data of Ranger and Nicholls[4] and the present study, however, is amazingly good, as shown in Figure 23. It may be observed that the model of a disk-shaped drop, while rather crude for a nearly spherical drop, is perhaps not unrealistic at later times when the drop has been considerably flattened.

3.3 CATASTROPHIC MODE

The dominant effect in the catastrophic mode is seen to be the rapid growth of surface waves on the windward face of the drop. Taylor[7] pointed out that when the direction of acceleration of a fluid interface is from the less dense fluid to the more dense, waves on the interface will be unstable and will grow exponentially. Small waves or irregularities are always present in any real physical situation, but when they are unstably amplified, they may grow so large that they tear the drop apart.

Taylor's theory[7] for the growth of the waves is strictly applicable only to small disturbances, but it may be interpreted as providing the relevant parameter for correlating the experimental data even though the wave amplitudes become very large (at the point of disintegration, the wave amplitudes are comparable in magnitude to the diameter of the drop itself). The theory predicts the following characteristic amplification time for the wave amplitudes:

$$t_c = \frac{\rho_L^{1/2}\,\sigma_L^{1/4}\,D_o^{3/4}}{\rho_2^{3/4}\,u_2^{3/2}}. \tag{24}$$

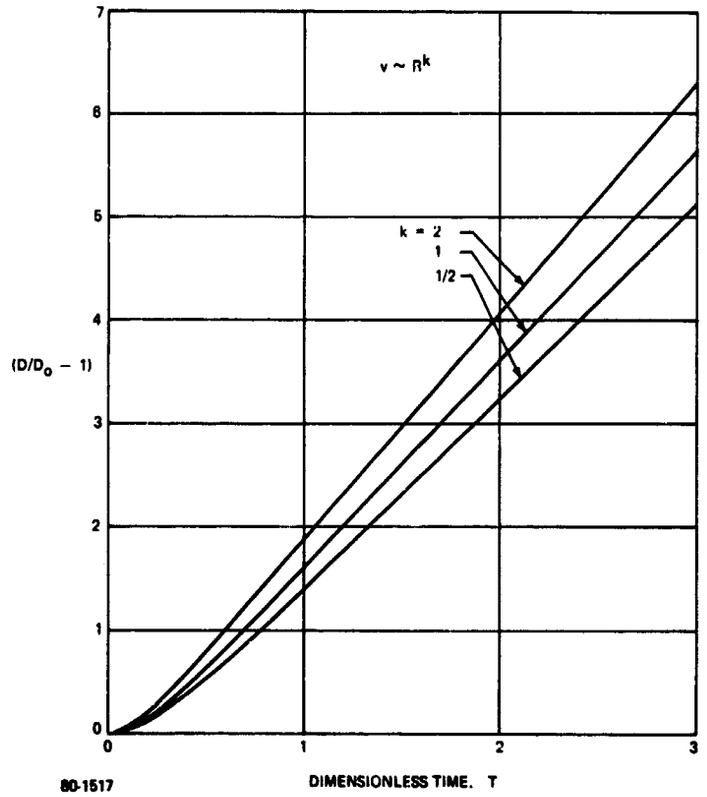

Figure 22 DISK-SHAPED DROP DEFORMATION

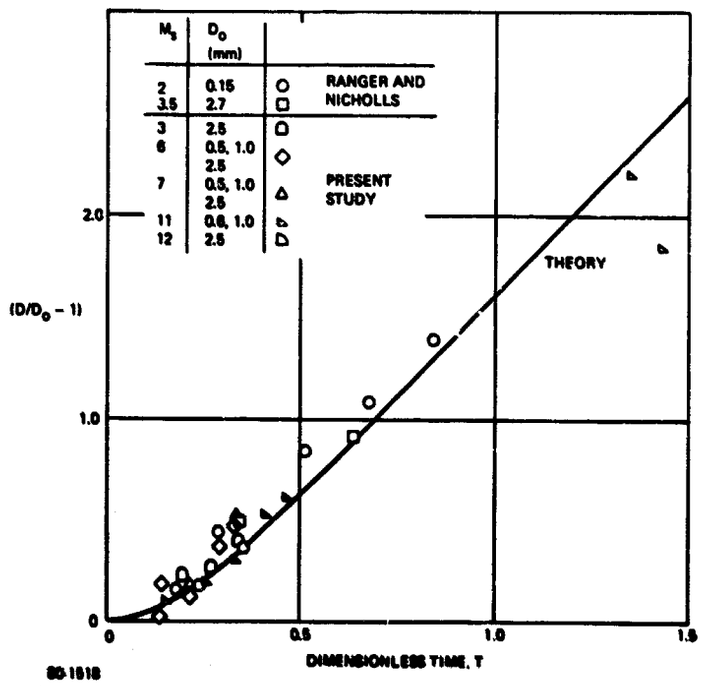

Figure 23 DROP DEFORMATION: HIGH-SPEED DATA

The corresponding nondimensional time is

$$T_c \propto \frac{\sigma_L^{1/4}}{\rho_2^{1/4}\, U_2^{1/2}\, D_o^{1/4}} \tag{25}$$

Hence the theory suggests the following correlation parameter for the catastrophic mode:

$$W \equiv \frac{\rho_2 U_2^2 D_o}{\sigma_L}, \tag{26}$$

which is the Weber number.

We now turn to the relevant experimental data. The variation of drop mass with time shown in Figures 17, 18, and 19 corresponding to tests at Mach 3, 6, and 11, respectively, indicates catastrophic breakup is occurring early (with respect to stripping effects) in the Mach 11 tests, at intermediate time at Mach 6, and late time (if at all) at Mach 3. In view of the analysis given above, it is appropriate to plot these breakup times versus the Weber number, W. The times to breakup in the three cases are 150, 50, and 22 msec, respectively, or in the dimensionless T_b form, 2.7, 2.0, and 1.4. These values of T_b are plotted versus W in Figure 24, and are seen to be well correlated by the equation

$$T_b = 45\, W^{-1/4} \tag{27}$$

Thus the theoretical analysis of the catastrophic mode appears well verified. Moreover, it appears that even the lowest Mach number data were subject to catastrophic breakup, but only after a substantial amount of stripping had occurred.

Further verification of this dependence of T_b on Weber number is available in the data of Reinecke and McKay.[5] They report high Weber number, catastrophic breakup data on the basis of their spark shadowgraphic measurements of time to breakup. These four relevant data are also plotted in Figure 24 and are reasonably well correlated by $W^{-1/4}$. Thus the spark shadowgraphic method of determining breakup time appears to give reliable qualitative results, but generally to overestimate breakup time by about a factor of two, at least in this high Weber number regime.

The values of Weber number employed in these calculations were based on the room-temperature value of the water surface tension σ_L. It may be objected that the surface of the drop is raised to much higher temperatures by aerodynamic heating in the shock-tube experiments, so that a lower value of σ_L should be used. We note, however, that the thermal layer in the water drop is extremely thin under transient experimental conditions, and that the choice of an appropriate value for σ_L depends (among other things) on considerations of the interaction of this thermal layer with the growing surface waves themselves. Such considerations are beyond the scope of this study.

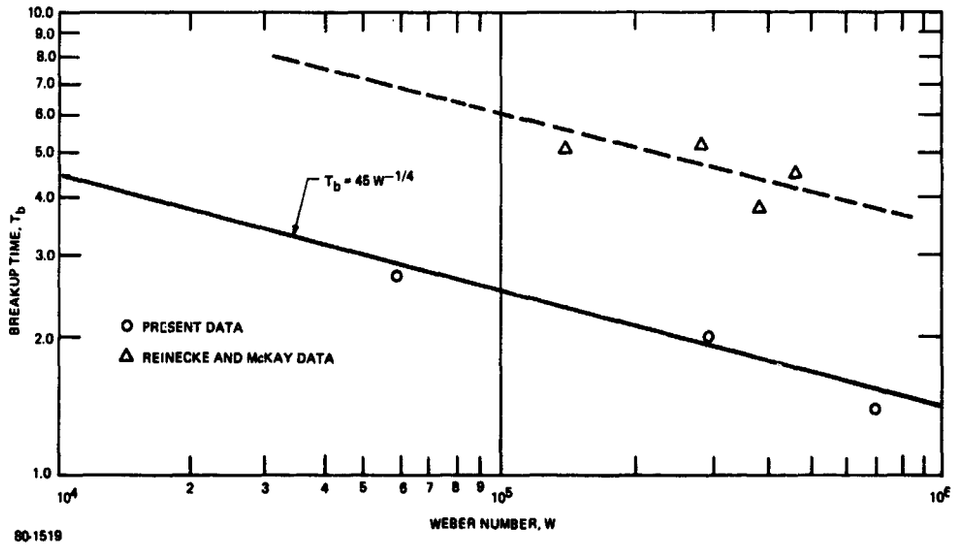

Figure 24 CORRELATION OF DATA WITH WEBER NUMBER

3.4 STRIPPING MODE

An analysis for the mass loss during stripping has been given by Taylor.[8] Taylor observed that the motion of the air over the surface of the drop tends to drag fluid along with it, and he assumed that such fluid might be spilled over, or separated, into the wake of the flow somewhere near the equator of the drop, where its velocity is greatest. His analysis did not go into the details of the spillage process, but simply required that the accelerated fluid (or some fraction thereof) in the boundary layer on the surface of the drop be ripped off in some manner when it reaches the equator. The problem then reduced to calculating the mass flow in the boundary layer, which varies as a function of the drop diameter, speed, etc.

There is an error in the Taylor analysis involving the position of the parameter A in the final result. Ranger and Nicholls[4] have corrected Taylor's error, and they report adequate agreement of the theory with their data. Although the deceleration of the drop can be included in the analysis, we shall start by applying Ranger and Nicholls' theoretical result to the case of no deceleration. The stripping analysis then predicts the following law of variation of the mass loss rate:

$$\frac{dm}{dt} = - (\pi D)^{3/2} \left(\frac{3}{2} \rho_L \mu_L u_2 A \right)^{1/2} \qquad (28)$$

where

$$A = \left(\frac{\rho_2 \mu_2}{\rho_L \mu_L}\right)^{1/3} . \tag{29}$$

For a spherical drop, the mass is related to the drop diameter by the equation

$$m = \frac{\pi}{6} \rho_L D^3 . \tag{30}$$

We then have, in terms of the nondimensional time,

$$\left(\frac{m}{m_o}\right)^{1/2} \frac{d}{dT}\left(\frac{m}{m_o}\right) = -3\sqrt{6\pi \frac{\mu_L A}{\rho_2 u_2 D_o}}, \tag{31}$$

which has the solution

$$1 - \left(\frac{m}{m_o}\right)^{1/2} = 6.5\, T \sqrt{\frac{\mu_L A}{\rho_2 u_2 D_o}} . \tag{32}$$

Hence, the relevant parameter for the stripping mode would be the "mixed Reynolds number"

$$R \equiv \frac{\rho_2 u_2 D_o}{\mu_L A} = \frac{\rho_2^{2/3} \rho_L^{1/3} u_2 D_o}{\mu_2^{1/3} \mu_L^{2/3}} . \tag{33}$$

The Mach 3 data shown in Figure 17 present the conditions under which stripping apparently progressed farthest until the onset of large instabilities. An extrapolation of these data suggests that, had stripping continued, the drop mass would have vanished at between 180 and 200 msec, i.e., at a value of T of about 3.5. The value of R for these conditions is approximately 94,000. If we substitute this value into Equation (33) and compute the nondimensional time corresponding to $m = 0$, we obtain $T = 47$, more than an order of magnitude greater than the experimental breakup time. It seems unlikely that any simple correction to the theoretical result would be sufficient to overcome such a large discrepancy. We are therefore led to the conclusion that the analysis developed by Taylor and corrected by Ranger and Nicholls does not represent a valid theoretical interpretation of the observed stripping of mass from water drops at high relative velocities; the mechanism of stripping must be roughly an order of magnitude more effective than that suggested by these authors.

We shall not attempt to provide a new analytical representation of the stripping mode in this report, but rather concentrate on obtaining a simplified correlation of the experimental data which will be adequate for flight predictions.

Further consideration of the Mach 3 data, as well as the Mach 6 results (Figure 18), indicates that stripping initially reduces the mass at a fairly slow rate and subsequently becomes more effective; i.e., dm/dt is small at early time. At the other extreme, i.e., when stripping is well established, we may postulate that the mass removal rate is proportional to the drop mass remaining, which would suggest that $dm/dt = 0$ at $t = t_s$, where the subscript s indicates breakup time due to stripping. Hence the curve $m(t)$ may be expected to have a small slope both at small time and near t_s. A simple curve satisfying these requirements is

$$\frac{m}{m_o} = \frac{1}{2}\left(1 + \cos \pi \frac{t}{t_s}\right). \tag{34}$$

Using a value of $t_s = 3.5$, this curve is shown along with the experimental mass histories in Figures 25, 26, and 27. The agreement with the data is good at all three test conditions. Note that no theoretical claim can be made concerning Equation (34). It is, however, a physically reasonable and accurate representation of the experimental data. Note also the apparent constant value of T_b.

We have plotted the lower Weber number data of Engel,[2] Nicholson,[3] and Ranger and Nicholls[4] versus R in Figure 28. We have also included our Mach 3 point with its estimated T_b due to stripping of 3.5. Although there appears to be a slight positive dependence of T_b upon R, the large scatter makes this questionable. In fact, Nicholson interpreted his own data as indicating a constant value for T_b of 3.5. The stripping analysis of Equation (32) is therefore open to serious question, since no dependence on the mixed Reynolds number can be inferred from the data.

With regard to choosing a working value for T_b due to stripping, we are inclined tentatively to conclude that it is 3.5 and constant. This value lies between the results of Engel and Ranger and Nicholls, is quoted by Nicholson on the basis of his more quantitative definition of drop breakup, and is compatible with our own estimated value on the basis of the X-ray data.

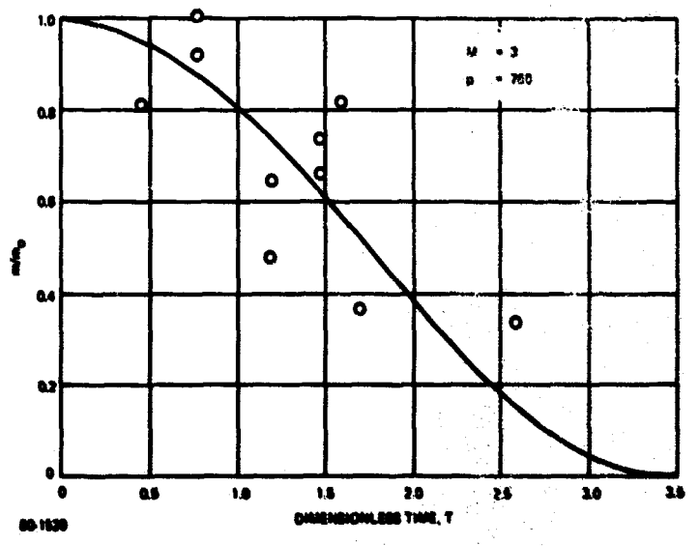

Figure 25 DROP MASS HISTORIES AT MACH 3

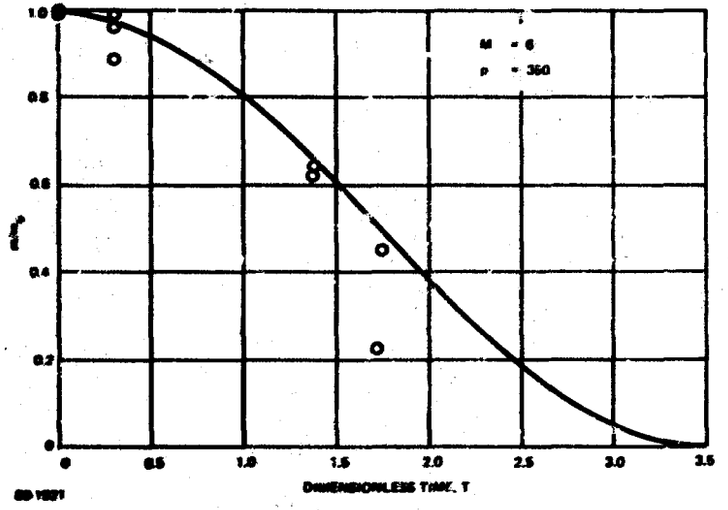

Figure 26 DROP MASS HISTORIES AT MACH 6

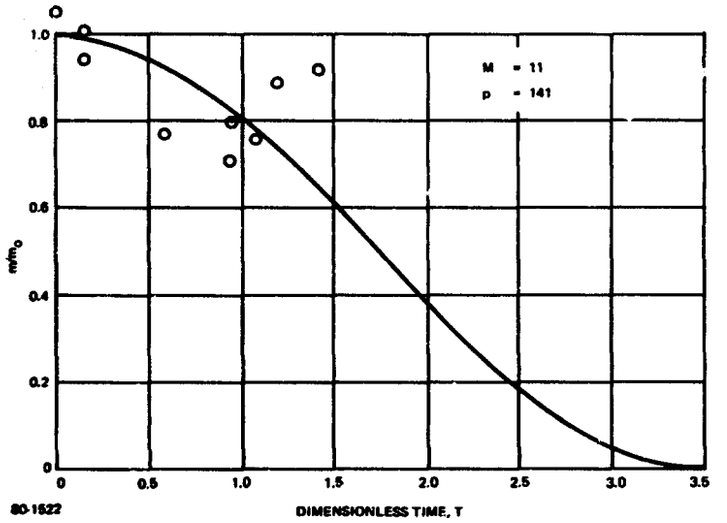

Figure 27 DROP MASS HISTORIES AT MACH 11

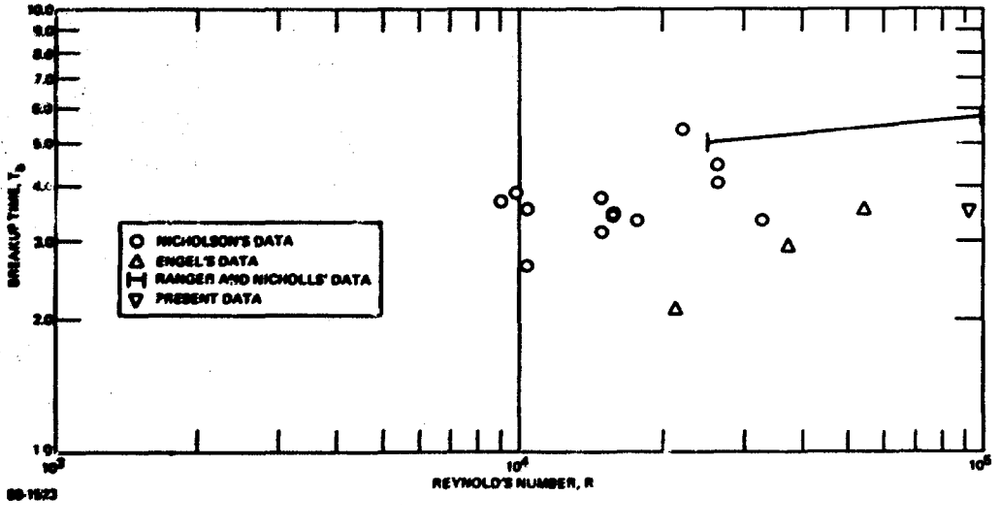

Figure 28 BREAKUP TIME FOR STRIPPING MODE

4.0 DROP BREAKUP CALCULATIONS UNDER FLIGHT CONDITIONS

Employing the experimental and theoretical criteria for drop breakup reported above, representative preliminary calculations have been made to assess the importance of drop breakup under realistic reentry conditions. The results suggest that the primary mode in the stagnation region is catastrophic breakup, while the stripping mode is dominant in the downstream region of the vehicle shock layer.

Drop breakup calculations are naturally divided into three parts. In the first part, the experimental correlation of drop deceleration in the shock tube is expressed in vehicle-fixed coordinates, and the nondimensional impact time is then computed as a function of drop diameter. In the second part, the drop breakup criteria are used to ascertain the appropriate nondimensional breakup time as a function of drop diameter. Finally, the two times are compared in order to determine the fraction of drop mass entering the shock layer which does not reach the vehicle surface as a function of drop diameter, and this function is integrated over the rainstorm drop mass distribution function to yield the net mass fraction.

Two cases have been considered: the stagnation region of a blunt-nosed body and the conical region far downstream of the nose. In the stagnation region, a reasonable estimate is obtained by considering only the breakup of drops which traverse the stagnation streamline. Although drops which traverse other parts of the shock layer will experience somewhat different flow conditions, the stagnation streamline provides representative conditions and is simple to analyze. Furthermore, a direct analogy relates the stagnation streamline problem to the experimental conditions in the shock tube: In a high-speed shock layer, the flow conditions along the stagnation streamline are virtually uniform and hence similar to the uniform-flow region behind the shock wave in the shock tube. In the downstream region, the disturbance caused by the blunt nose tends to die out, and the flow field becomes approximately conical. High-speed conical shock layers are also characterized by approximate uniformity, and similarity with experimental conditions can be established if the relative drop motion in the direction perpendicular to the vehicle surface is considered.[9] Although it is possible to consider more complicated, non-uniform flow fields, this is beyond the scope of the present effort.

In shock-tube coordinates, the distance between the shock wave and the drop is given by

$$s = u_s t - x, \tag{35}$$

where x is the distance the drop has moved from its original position. In nondimensional variables, the experimental drop acceleration correlation is

$$X = 0.8\, T^2. \tag{36}$$

Since

$$\rho_2 = \rho_\infty/\epsilon,$$

$$u_2 = (1-\epsilon)\, u_s, \tag{37}$$

Equation (35) can be written

$$S = B\,T - 0.8\,T^2, \tag{38}$$

where

$$B = \frac{1}{1-\epsilon}\sqrt{\frac{\epsilon}{b_\infty}},$$

$$b_\infty = \rho_\infty/\rho_L. \tag{39}$$

This equation has the solution

$$T = \frac{B}{1.6}\left(1 - \sqrt{1 - 3.2\,\frac{S}{B^2}}\right). \tag{40}$$

In relating this equation to the case of flight through the atmosphere, we interpret u_s as the flow velocity component normal to the shock wave: in the stagnation region, the free-stream velocity V_∞; in the conical-flow region, the velocity $V_\infty \sin\theta_s$, where θ_s is the inclination of the shock wave. In what follows, we shall be concerned only with conditions at impact on the vehicle surface. In the stagnation region, the nondimensional distance S is then interpreted as Δ/D_o, where Δ is the shock standoff distance, related to the nose radius R_N and the shock density ratio ϵ by the high-speed correlation[9]

$$\Delta \simeq 0.78\,\epsilon\,R_N. \tag{41}$$

In the conical-flow region, S is interpreted as the perpendicular distance from the shock wave to the body $L = R_i \sin(\theta_s - \theta_c)$, where R_i is the distance from the cone vertex at which the drop strikes the vehicle surface. We can evaluate L by the high-speed correlation[9]

$$L \simeq 0.6\,\epsilon\,\theta_s\,R_i. \tag{42}$$

Here θ_c is the inclination of the vehicle surface. For the two regions, Equation (40) then gives the impact time in the form

$$T_i = \begin{cases} \dfrac{B}{1.6}\left(1 - \sqrt{1 - Z_N\,\dfrac{R_N}{D_o}}\right), & \text{nose} \\ \dfrac{B}{1.6}\left(1 - \sqrt{1 - Z_c\,\dfrac{R_i}{D_o}}\right), & \text{cone} \end{cases} \tag{43}$$

where

$$Z_N = 2.5\,(1-\epsilon)^2\,b_\infty$$

$$Z_c = 1.92\,(1-\epsilon)^2\,b_\infty\theta_s. \tag{44}$$

It is therefore seen that, for given flight conditions and for a given θ_s , the nondimensional impact times are functions only of the ratios R_N/D_o and R_i/D_o .

We have considered three altitudes (0, 15, and 30 kft) and three flight Mach numbers (5, 10, and 20). Figures 29, 30, and 31 show the impact time in the nose region as a function of R_N/D_o for these conditions. For impact downstream on the vehicle, we have considered three cone angles (θ_c = 5, 10, and 15 degrees). Instead of plotting the corresponding impact time from Equation (43) for all 27 cone conditions, we note that for values of B greater than about 30, the acceleration term $0.8\,T_i^2$ is very small and can be dropped from Equation (38); the impact time is then simply given by the relationship

$$T_i = C\,\frac{R_i}{D_o} \quad , \tag{45}$$

where

$$C = 0.6\,\frac{\epsilon\,\theta_s}{B} \tag{46}$$

For those cases in which this relationship is valid, the factor C is tabulated in the following table.

C

θ_c (deg)	M_∞	h = 0	h = 15 kft	h = 30 kft
5	5	0.373	0.298	0.228
	10	0.846	0.671	0.517
	20		0.68	0.525
10	5	1.71	1.35	1.05
	10		1.38	1.07
15	5	2.72	2.16	1.66

The experimental breakup criteria which we have used are as follows: If the impact time T_i is greater than the breakup time T_b, the drop mass at impact is taken to be zero. If the impact time is less than the breakup time, the drop mass at impact is given by the stripping-mode correlation

$$\frac{m_s}{m_o} = \frac{1}{2}\left(1 + \cos \pi\,\frac{T}{3.5}\right) \tag{47}$$

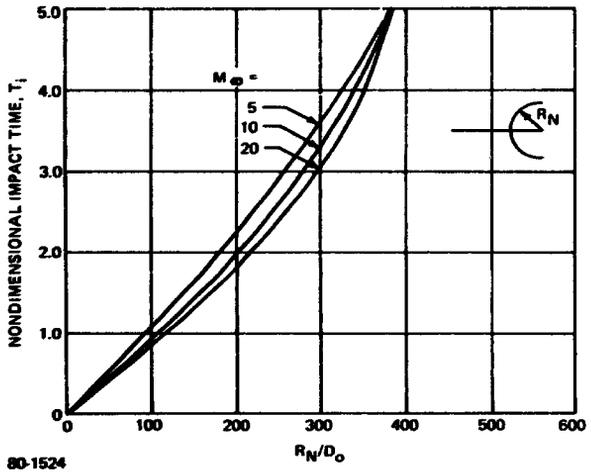

Figure 29 TIME TO IMPACT STAGNATION POINT, h = 0

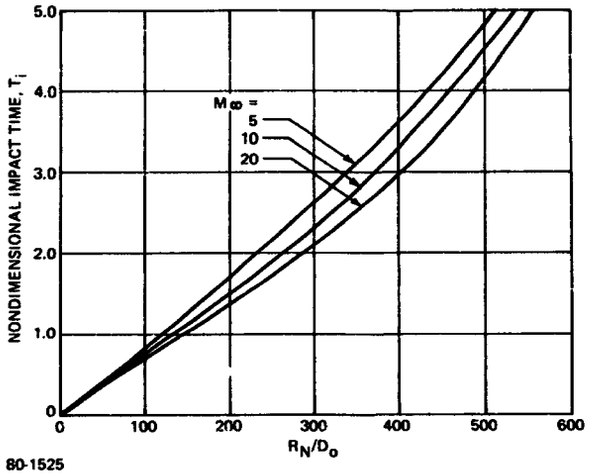

Figure 30 TIME TO IMPACT STAGNATION POINT, h = 15 kft

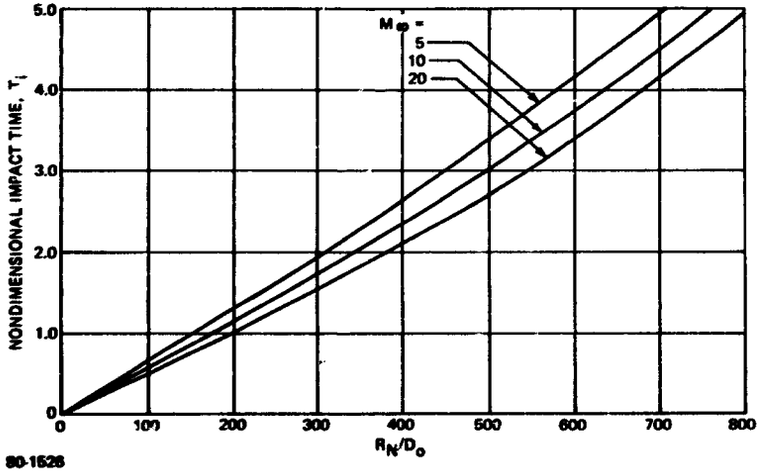

Figure 31 TIME TO IMPACT STAGNATION POINT, h = 30 kft

where m_o is the initial mass. The breakup time is taken to be the smaller of 3.5 (stripping mode) and $45\,W^{-1/4}$ (catastrophic mode), where

$$W = \frac{\rho_2\, u_2^2\, D_o}{\sigma_L} = \frac{(1-\epsilon)^2}{\epsilon}\, W_\infty \sin^2\theta_s,$$

$$W_\infty = \frac{\rho_\infty\, V_\infty^2\, D_o}{\sigma_L} \qquad (48)$$

It should be noted that the range of experimental data which led to the latter correlation for catastrophic breakup is exceeded somewhat under flight conditions in the stagnation region.

We have only considered the case $M_\infty = 10$ at 15 kft altitude in the detailed breakup calculation below. At that altitude, there is a peak in the rainstorm water content for the particular model which we chose (described below), so that these conditions are representative of a severe rain environment. We chose representative nose radii of 0.02, 0.1 and 0.5 foot, and in the conical-flow region we chose a 10-degree half-angle cone with $R_i = 1$ and 5 feet. (These values essentially designate the axial location of the impact points.) The standoff distance Δ for these conditions is about 0.002, 0.01, and 0.05 foot, respectively ($\Delta / R_N = 0.0975$, $\epsilon = 0.125$).

Figure 32 shows the impact times for the designated conditions as functions of the dimensionless distances. Figures 33 and 34 show the impact and breakup times as functions of the initial drop diameter (D_o) in millimeters for the four cases. Figure 33 shows that the breakup time in the nose region is essentially dominated by the catastrophic mode. We observe that in the nose region, drops with diameters less than 0.17 mm do not reach the surface of the 0.1-foot-radius nose, while for the 0.5-foot-radius nose the breakup effect is much more important: drops smaller than 1.4 mm diameter are dissipated.

In the conical-flow region (see Figure 34), although the catastrophic mode affects the results for the 5-foot station slightly, the stripping mode largely controls the amount of mass reaching the surface. At the 1-foot station, drops with diameters smaller than 0.12 mm are completely dissipated before they reach the surface, while at the 5-foot station the corresponding diameter is 0.7 mm. We chose as a rainstorm model a typical summer storm referred to in the Air Force Handbook of Geophysics[10] as Case I. This case is believed to be representative of a summer rain in temperate latitudes, and to come close to simulating widespread tropical rains. It was derived by combining empirical and theoretical data indicating approximate weather conditions in this type of storm. The maximum updraft was taken to be 0.2 m/sec yielding a precipitation rate of 0.2 in./hr. Such a rate would be exceeded in Washington, D.C., about 40 hours in an average year and could probably be referred to as a medium rain. The precipitation rate will not enter directly into these calculations, however; the results will be given in terms of the mass fraction of the incoming rain that reaches the vehicle surface, so that the impinging mass rate per surface area of the vehicle must be determined by multiplying by the rain concentration, the vehicle velocity, and the surface inclination. At 15 kft altitude, the rain concentration for this storm is about 1 gm/m^3, giving an incoming mass rate of about 0.02 slug/ft^2-sec.

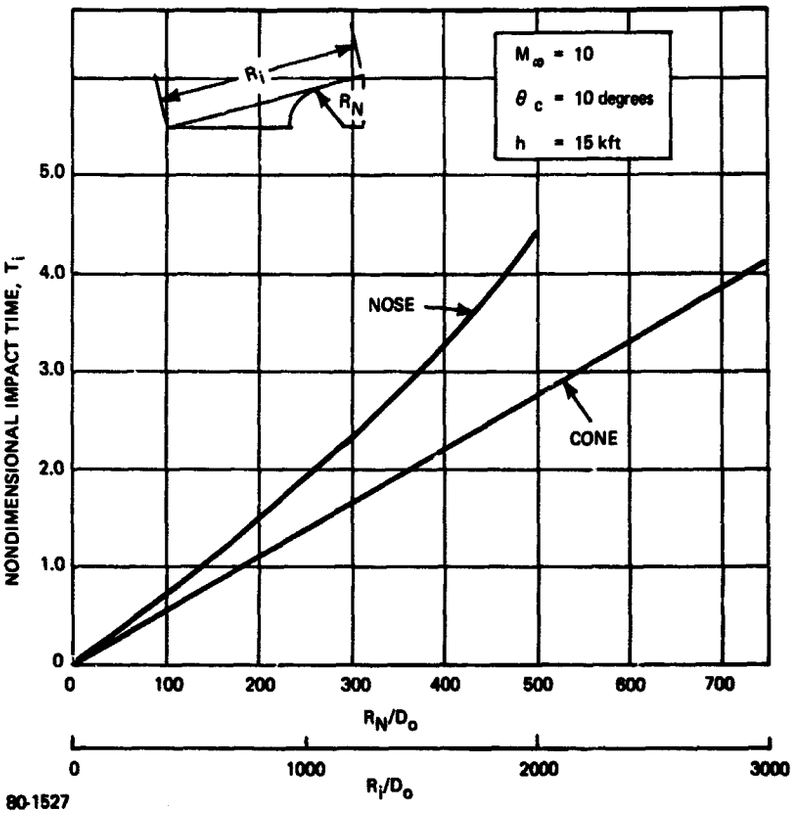

Figure 32 NOSE AND CONE IMPACT TIMES

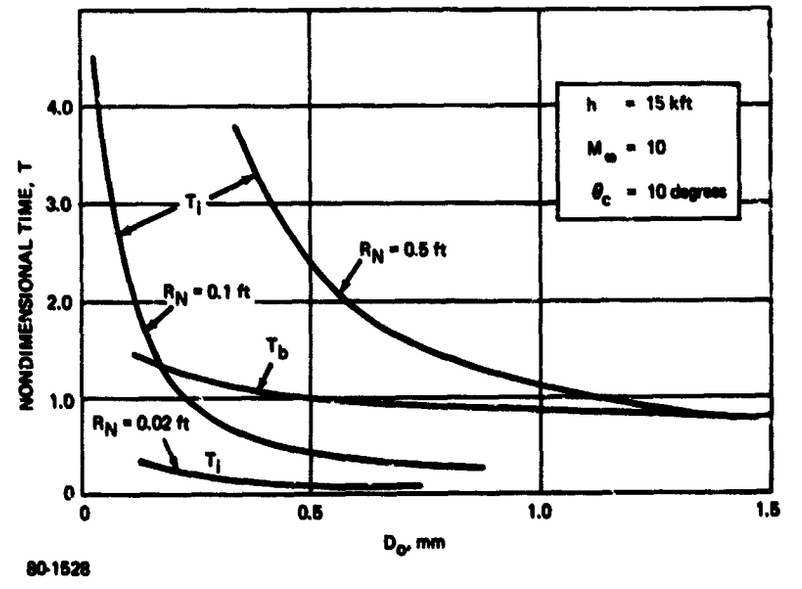

Figure 33 IMPACT AND BREAKUP TIMES FOR NOSE

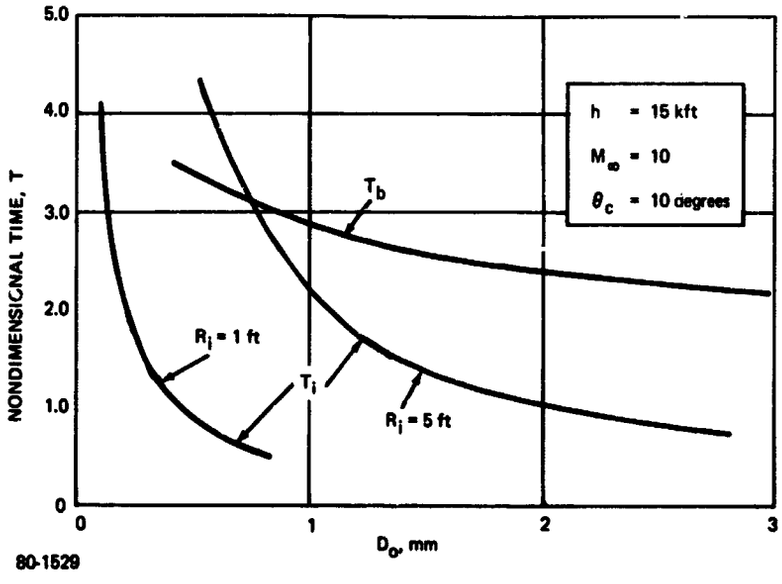

Figure 34 IMPACT AND BREAKUP TIMES FOR CONE

Reference 10 (page 6-9) gives an expression for the raindrop size distribution function which can be converted into the following mass distribution function:

$$\mu = \frac{1}{6D_R}\left(\frac{D}{D_R}\right)^3 e^{-D/D_R} \quad . \tag{49}$$

Here μdD is the mass fraction of drops with diameters between D and $D + dD$, and the reference diameter D_R is related to the reference diameter "D_o" in Reference 10 by

$$D_R = "D_o"/3.67 \tag{50}$$

This distribution function is shown plotted in Figure 35. The reference diameter D_R is a weak function of the precipitation rate[10]; in this case, $D_R = 0.255$ mm.

It should be noted that this model storm takes into account only precipitating rain and neglects the cloud water content, which in general is significantly greater than the precipitating water content. The cloud water is also distributed over much smaller particles, so that the shock layer effect on the cloud water should be more pronounced than on the precipitating water.

The mass fraction of drops with diameters between 0 and a given diameter D_1 can be determined by integrating Equation (49) between the respective limits:

$$M_1 = \int_0^{D_1} \mu dD = P(4, \bar{D}_1) , \tag{51}$$

where

$$P(4, \bar{D}_1) = 1 - \left[1 + \bar{D}_1 + \frac{1}{2}(\bar{D}_1)^2 + \frac{1}{6}(\bar{D}_1)^3\right] e^{-\bar{D}_1} ,$$

$$\bar{D}_1 = D_1 / D_R \tag{52}$$

We have computed the mass fraction, M_i, of drop mass which strikes the surface. In the nose region this can be accomplished with reasonable accuracy by evaluating Equation (51) in terms of the diameter D_1 of the smallest particle to reach the surface, previously cited; then $M_i = 1 - M_1$. The impact times are generally so low that there is no significant effect of stripping on the remaining drops. In the conical-flow region, however, such an estimate would disregard the fact that a significant fraction of the drops which do reach the surface have had part of their mass stripped off. The corresponding mass fraction lost must be computed by applying Equation (47) to the mass distribution function and integrating over the remaining drops. The total impinging mass fraction then becomes

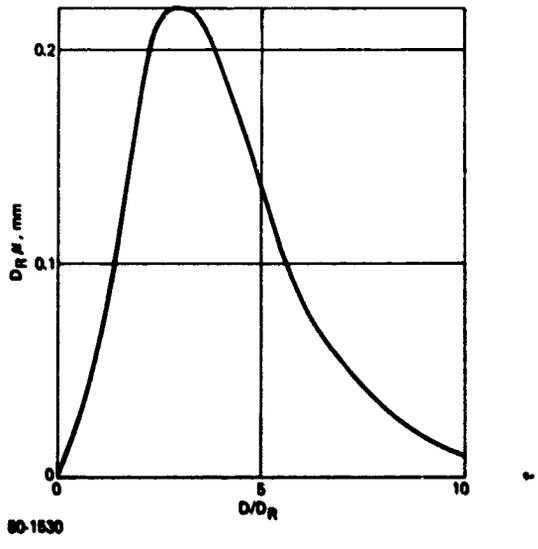

Figure 35 RAINSTORM MASS DISTRIBUTION FUNCTION

$$M_i = 1 - M_1 + \int_{D_1}^{\infty} \frac{m_s}{m_o} \mu dD \tag{53}$$

where D_1 is the drop diameter for which $T_i = T_b$. To facilitate this computation, a digital computer program has been written.

The results of the mass removal calculations are summarized in the following table for both the nose and cone regions.

M_∞ 10, h = 15 kft, θ_c 10 degrees

		Critical Drop Diameter, D_1 (mm)	Impinging Mass Fraction, M_i
Nose	R_N = 0.02 ft	0.02	1.00
	R_N = 0.1 ft	0.17	0.97
	R_N = 0.5 ft	1.4	0.22
Cone	R_i = 1 ft	0.12	0.92
	R_i = 5 ft	0.75	0.29

Clearly for the 0.02- and 0.1-foot-radius nose and 1-foot station on the cone, the drops lose virtually none of their mass, and the impinging mass on the surface at these points will comprise nearly all the mass which has entered the shock layer at the corresponding points. For the 0.5-foot-radius nose, very little mass strikes the vehicle surface at the stagnation point, and the vehicle shock layer is 78 percent efficient in protecting the surface from the rain. At the 5-foot station on the cone, 71 percent of the entering rain mass will be dissipated through the mechanism of drop breakup.

Figure 36 shows details of the impinging drop mass fraction as a function of drop diameter (in microns) for the 0.02-foot-radius nose. It may be noted that for this small nose radius, the stripping mode becomes important for drop diameters very near the cutoff diameter--20 microns--for catastrophic breakup. Since our predictions are based on correlations of data obtained for much larger drop sizes, additional experimental work would be required to verify this interesting conclusion and to pin down the critical drop breakup parameters for very small droplets.

Figures 37 through 39 show drop impact velocities and angles as functions of drop diameter, D_o. The drop impact velocity components normal to the body surface were obtained by differentiating the experimental drop acceleration correlation, Equation (36). The impact angles were obtained from the impact velocity component normal to the surface together with the component tangential to the surface; the latter was assumed unchanged during passage through the shock layer.

It can be concluded that drop breakup effects are potentially important in high-speed shock layers. Depending on the flight conditions and vehicle configuration, a large fraction of the entering drop mass may be dissipated in the shock layer, never reaching the vehicle surface. In the stagnation region, the catastrophic breakup mode is extremely important. Correlations of the experimental data presented in this report can be used to make detailed predictions of raindrop breakup effects for reentry vehicles.

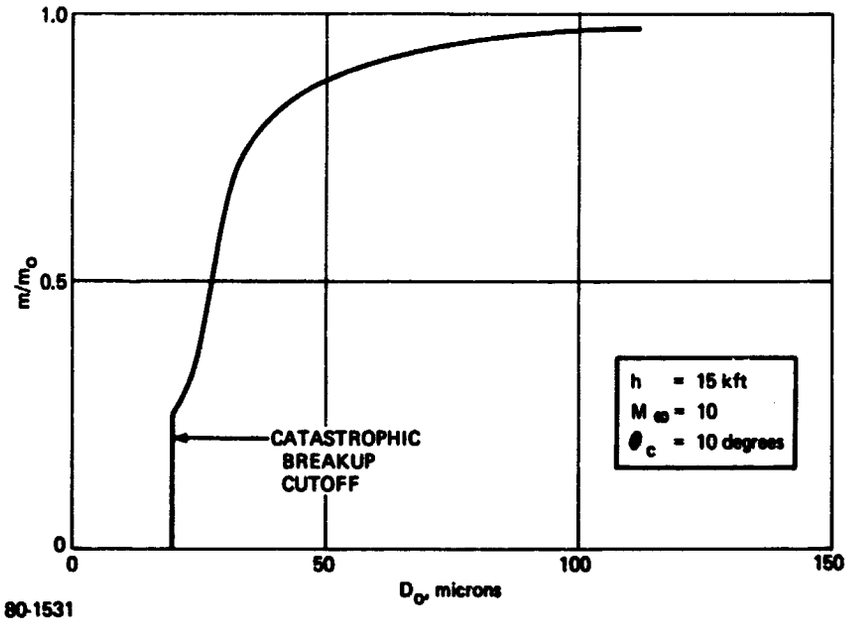

Figure 36 IMPINGING DROP MASS FRACTION VERSUS DIAMETER FOR 0.02-FOOT-RADIUS NOSE

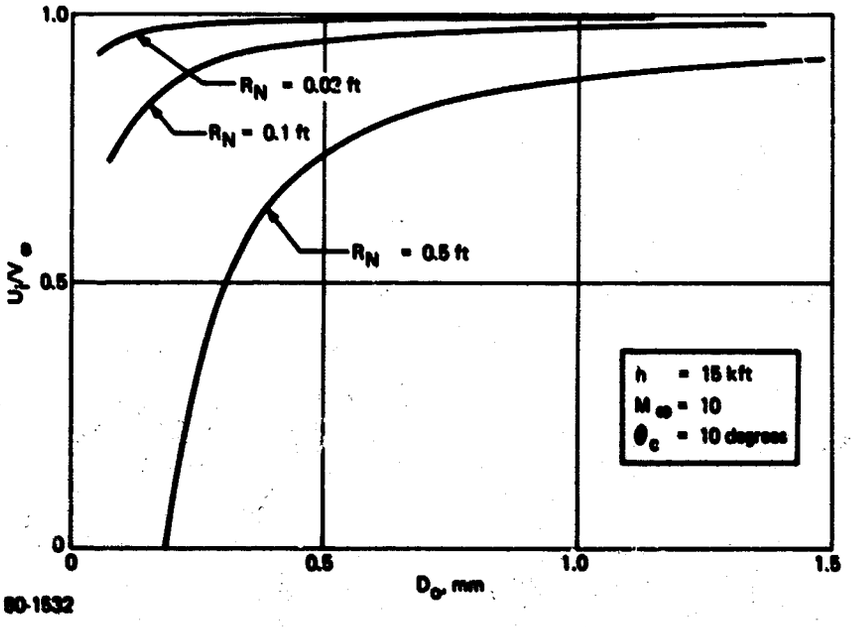

Figure 37 IMPACT VELOCITY FOR NOSE

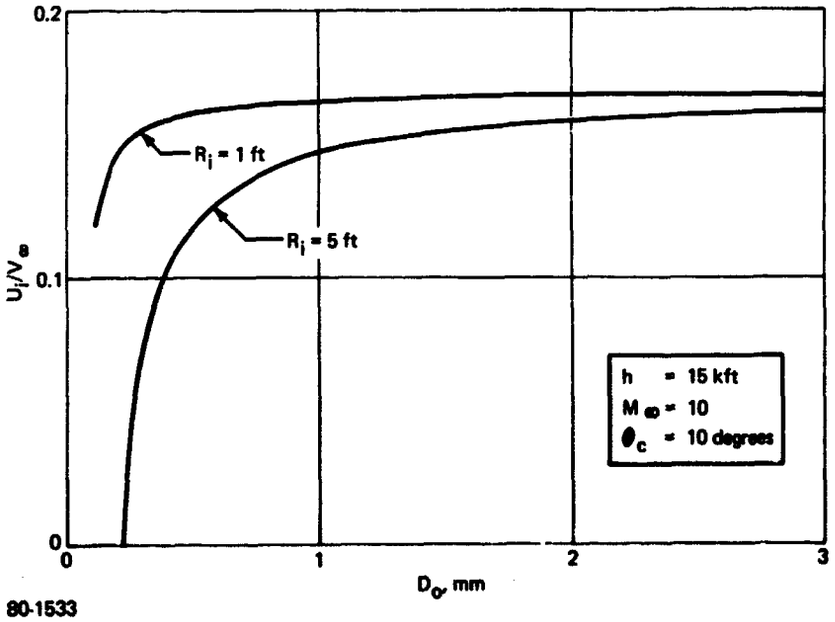

Figure 38 NORMAL VELOCITY AT IMPACT FOR CONE

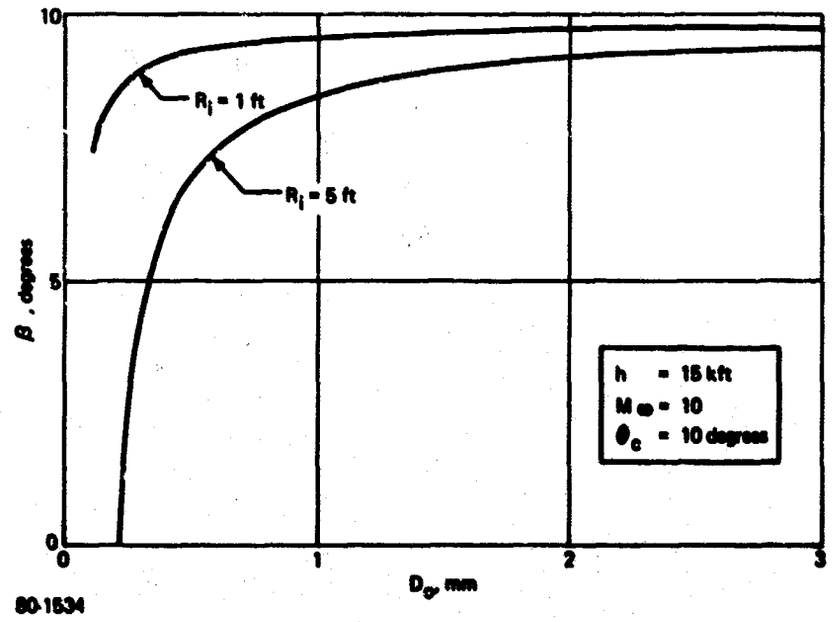

Figure 39 IMPACT ANGLE FOR CONE

5.0 SUMMARY AND CONCLUSIONS

An experimental program has been carried out to determine the modes of raindrop breakup in air after passage of a strong shock wave. Relevant dimensionless parameters have been determined, and the experimental data have been used to determine raindrop breakup in the shock layer of a reentering vehicle passing through a rainstorm.

The raw experimental data consisted of both shadowgraphs and X-ray photographs of disintegrating waterdrops in a shock tube. Data were taken for a range of drop diameters from 0.5 to 2.5 mm, for ambient pressure levels from 140 to 760 torr, and for shock Mach numbers from 3 to 11. The X-ray photographs were taken by doping the drops to saturation with lead acetate. The motivation behind using X-ray photography was to obtain reliable data on the drop mass remaining at late stages in the disintegration process, when the cloud of mist previously torn from the drop totally obscures the drop contour on a shadowgraph. In the regime dominated by catastrophic breakup, the X-ray results show qualitative agreement with conventional spark shadowgraph data, but indicate about half of the times to breakup obtained from the shadowgraph method. Determination of the mass remaining in the drops was accomplished by processing the X-ray negatives with a microdensitometer, and then integrating the resulting output digitally.

Examination of the shadowgraphs demonstrated conclusively that material was being stripped from the drops continuously at all test conditions. At the more severe test conditions, a second "catastrophic" mode of breakup became dominant, and the drop was shattered before all its material could be removed by stripping. The catastrophic mode of breakup is related to the unstable growth of waves on the front surface of the drop caused by the rapid acceleration of the drop by the air stream. In this mode, surface waves are observed to grow rapidly until their amplitude is comparable to the dimensions of the drop, at which point the drop is torn apart.

An additional effect which is superimposed on these two modes of breakup is the initial flattening of the drop caused by the imposed pressure differential between the poles and the equator. Because the deformation of the drop may affect the breakup process, shadowgraphs were taken at the early stages of the process to determine the rate of deformation. The deformation of the drop also affects its trajectory, since the drag coefficient cannot be considered to remain constant. In making flight predictions, it was decided to rely on the experimental data for information on the drop trajectory, and these data were therefore reduced and correlated.

Earlier investigators have found that the data on drop trajectories could be correlated by the relationship

$$X \quad 0.8\,T^2$$

where X and T are dimensionless shock-tube distance and time, respectively. The data on initial drop deformation were at variance with Burgers' analytical result,

but could be correlated by a simplified analytical model involving the assumption of a disk-shaped drop. The failure of the early-time analysis to predict the drop deformation is apparently due to the fact that the range of applicability of the early-time assumption is vanishingly small.

The catastrophic-mode data, obtained from the X-ray photographs, could be correlated by the formula

$$T_b = 45\ W^{-1/4}$$

where T_b is the time to breakup and W is the Weber number. This variation is in accord with the small-disturbance theory for unstable waves.

It was decided to take the dimensionless time to breakup for the stripping mode equal to 3.5, based on the experimental data. This was done with some reluctance, since the theory for stripping predicts a variation for T_b as the 1/2-power of the mixed Reynolds number defined by Equation (31). There was however insufficient data to justify such a conclusion, and the available experimental data are reasonably correlated by the value 3.5. The data for the mass loss during the stripping process could be correlated by the formula

$$\frac{m}{m_o} = \frac{1}{2}\left(1 + \cos \pi \frac{T}{3.5}\right)$$

where m_o is the initial mass of the drop and m is the mass of the drop at the dimensionless time T.

Employing these correlations, calculations of the dissipation of raindrop mass in the shock layer of a reentering vehicle have been carried out. The relationship between the experimental setup and the passage of drops through the blunt-nose region and through the downstream conical-flow region has been determined, and the appropriate transformations have been made. Dimensionless impact times have been calculated for a number of flight conditions. The specific case of drop breakup during flight through the 15 kft level of a representative rainstorm has been considered. It was determined that for a 0.1-foot nose radius and for the 1-foot station on a 10-degree cone, essentially no mass is lost by the raindrops before they strike the surface of the vehicle. For a 0.5-foot nose radius, most of the incoming drop mass is dissipated, and the dominant mechanism for breakup is the catastrophic mode. At the 5-foot station on the 10-degree cone, about half of the incoming drop mass is dissipated; the dominant mechanism here is the stripping mode.

We conclude that computations of raindrop breakup in vehicle shock layers can be carried out under realistic conditions using the data, techniques, and correlations developed in this report. Two modes of drop breakup have been found to be important for high-speed flow. In the blunt-nose region the catastrophic mode of breakup appears to be dominant, while in the downstream flow region the stripping mode is the primary mechanism.

6.0 REFERENCES

1. Dabora, E., Production of Monodisperse Sprays, Review of Scientific Instruments, Vol. 28, No. 4, pp. 502-06 (April 1967).

2. Engel, O. G., Fragmentation of Waterdrops in the Zone behind an Air Shock, Journal of Research of the NBS, Vol. 60, No. 3, (March 1958).

3. Nicholson, J., Drop Breakup by Airstream Impact, Published in Rain Erosion and Associated Phenomena, RAE Report N68-19401-427, Farnborough, England (1967).

4. Ranger, A. and J. Nicholls, Aerodynamic Shattering of Liquid Drops, AIAA Journal, Vol. 7, No. 2 (February 1969).

5. Reinecke, W. G. and W. L. McKay, Experiments on Water Drop Breakup behind Mach 3 to 12 Shocks, Sandia Report to be published.

6. Ho, P. Y., Dynamics of Bag-Type Breakup of Droplets in Various Flow Fields, Ph.D. Thesis, Purdue University (January 1969).

7. Taylor, G. I., The Instability of Liquid Surfaces when Accelerated in a Direction Perpendicular to their Planes. I., Proc. Roy. Soc. A, Vol. CCI, pp. 192-196; (1950) reprinted in Scientific Papers, Vol. III, Cambridge University Press (1963).

8. Taylor, G. I., The Shape and Acceleration of a Drop in a High-Speed Air Stream, Advisory Council on Scientific Research and Technical Development, Ministry of Supply (1949); reprinted in Scientific Papers, Vol. III, Cambridge University Press (1963).

9. Waldman, G. D. and W. G. Reinecke, Particle Trajectories, Heating and Breakup in Hypersonic Shock Layers, AIAA Paper No. 69-712 (1969).

10. Air Force, Handbook of Geophysics, Revised Edition, Macmillan (1960).

APPENDIX

TABLE OF EXPERIMENTAL DATA

Shadowgraph Data: Test liquid was distilled water except where asterisk indicates saturated lead acetate solution.

Nominal Initial Drop Diameter (mm)	Nominal Shock Mach Number	Initial Pressure (torr)	Normalized Drop Diameter	Dimensionless Time after Shock Passage
1.0	6	350	1.00	0
1.0	6	350	1.035	0.14
1.0	6	350	1.12	0.22
1.0	9	350	1.21	0.26
1.0	11	140	1.30	0.33
1.0	11	140	1.62	0.46
2.5	6	350	1.37	0.29
0.5	6	350	1.18	0.14
0.5	9	350	1.52	0.34
0.5	11	140	2.84	1.43
0.5	11	140	3.20	1.34
0.5	11	140	3.50	1.88
0.5	11	140	3.25	2.50
0.5	11	140	Gone	2.75
0.5	11	140	1.12	0.15
2.5	6	350	1.47	0.33
2.5	9	350	1.18	0.22
2.5	12	90	1.54	0.41
2.5	3	350	1.23	0.20
2.5	3	350	1.39	0.34
2.5	3	350	1.27	0.27
1*	6	350	1.63	0.40
1*	6	350	3.57	1.28
1*	6	350	4.01	3.25
1*	6	350	3.40	2.56
1*	6	350	2.38	4.02
1*	6	350	4.14	3.68
1*	6	350	2.49	0.78
1*	6	350	1.44	0.30
1*	6	350	2.99	2.31

X-Ray Data: Test liquid was saturated lead acetate solution

Nominal Initial Drop Diameter (mm)	Nominal Shock Mach Number	Initial Pressure (torr)	Normalized Drop Diameter	Dimensionless Time after Shock Passage
2.12	6	350	0.99,1.00	0
2.12	6	350	0.62,0.64	1.38
2.12	6	350	0.45	1.95
2.12	6	350	0.23	1.99
2.12	6	350	0.99,0.89, 0.96	0.31
2.12	3	760	1.01	0.76
2.12	3	760	0.92	0.76
2.12	3	760	0.81	0.45
2.12	3	760	0.48	1.28
2.12	3	760	0.66,0.74	1.46
2.12	3	760	0.34	2.58
2.12	3	760	0.82	1.59
2.12	3	760	0.37	1.68
2.12	3	760	0.65	1.19
2.12	11	141	1.01,0.94	0.15
2.12	11	141	1.05	0
2.12	11	141	0.92	1.32
2.12	11	141	0.89	1.19
2.12	11	141	0.76	1.07
2.12	11	141	0.77	0.57
2.12	11	141	0.71,0.80	0.94

Unclassified

Security Classification

DOCUMENT CONTROL DATA - R & D

(Security classification of title, body of abstract and indexing annotation must be entered when the overall report is classified)

1. ORIGINATING ACTIVITY (Corporate author) Avco Government Products Group, Avco Systems Division 201 Lowell Street Wilmington, Massachusetts 01887	2a. REPORT SECURITY CLASSIFICATION Unclassified 2b. GROUP

3. REPORT TITLE

A STUDY OF DROP BREAKUP BEHIND STRONG SHOCKS WITH APPLICATIONS TO FLIGHT

4. DESCRIPTIVE NOTES (Type of report and inclusive dates)

Final Report

5. AUTHOR(S) (First name, middle initial, last name)

W. G. Reinecke
G. D. Waldman

6. REPORT DATE	7a. TOTAL NO. OF PAGES	7b. NO. OF REFS
May 1970	68	none

8a. CONTRACT OR GRANT NO.	9a. ORIGINATOR'S REPORT NUMBER(S)
F04701-68-C-0035	AVSD-0110-70-RR
b. PROJECT NO.	
c.	9b. OTHER REPORT NO(S) (Any other numbers that may be assigned this report) SAMSO-TR-70-142
d.	

10. DISTRIBUTION STATEMENT

This document may be further distributed by any holder only with specific prior approval of Space and Missile Systems Organization (SMYSE), Norton AFB, California 92409.

11. SUPPLEMENTARY NOTES	12. SPONSORING MILITARY ACTIVITY
The distribution of this report is limited because it contains technology requiring disclosure only within the Department of Defense.	SAMSO, Deputy for Reentry Systems Air Force Systems Command Norton AFB, California 92409

13. ABSTRACT

An experimental program has been carried out to determine the modes of raindrop breakup in air after passage of a strong shock wave. Relevant dimensionless parameters have been determined, and the experimental data have been correlated in terms of these parameters. The resulting correlations have been used to determine raindrop breakup in the shock layer of a reentering vehicle passing through a rainstorm.

DD FORM 1 NOV 68 1473

Unclassified

Security Classification

14 KEY WORDS	LINK A		LINK B		LINK C	
	ROLE	WT	ROLE	WT	ROLE	WT
Raindrop breakup						
Erosion						